LE

NASA Contractor Report 175037

Viscous Compressible Flow Direct and Inverse Computation With Illustrations

Tah-Teh Yang and Francois Ntone
Clemson University
Clemson, South Carolina

January 1986

Prepared for
Lewis Research Center
Under Grant NAG 3-538

NASA
National Aeronautics and
Space Administration

TABLE OF CONTENTS

List of Nomenclature

A	matrix defined on page 13 or variable in turbulence model in page 19.
$\tilde{A}$	matrix defined on page 15.
B	matrix defined on page 13.
$\tilde{B}$	matrix defined on page 15.
C_{cp}	constant in turbulence model on page 20.
C_{kleb}	constant in turbulence model on page 20.
C_p	specific heat at constant pressure.
C_v	specific heat at constant volume.
C_{wk}	constant in turbulence model in page 20.
C_2	constant defined on page 7.
D	matrix defined in Appendix B.
E	matrix defined in Appendix B.
$\underline{\underline{E}}$	matrix defined in Appendix C.
F	matrix defined in Equation (1).
F_1	matrix defined in Equation (1).
$\overline{F}$	matrix defined in Equation (2).
$\overline{F}_1$	matrix defined in Equation (2).
$\hat{F}$	matrix defined in Equation (4).
$\underline{F}$	vector defined in Appendix C.
F_{kleb}	Function in turbulence model on page 20.
F_{wake}	Function in turbulence model on page 20.
$F(y)$	Function defined on page 20.
G	matrix defined in Equation (1)
G_1	matrix defined on page 6.
$\overline{G}$	matrix defined in Equation (2).
$\overline{G}_1$	matrix defined on page 9.

$\hat{G}$	matrix defined in Equation (4).
$\hat{G}_1$	matrix defined on page 11.
$\hat{G}'$	matrix defined on page 11.
$\hat{G}_1'$	matrix defined on page 12.
H	matrix defined on page 6 or the height between two plates in Couette flow.
$\overline{H}$	matrix defined in Equation (2).
$\hat{H}'$	matrix defined on page (2).
I	identity matrix
J	Jacobian defined on page 9.
K	variable defined in Equation (12).
L	matrix defined in Equation (12).
M	Mach number
$\overline{M}$	matrix defined in Appendix B.
$\overline{M}_1$	matrix defined in Appendix B.
N	matrix defined in Equation (12).
Pr	Prandtl number
Pr_t	turbulent Prandtl number
Q	matrix defined in Equation (12).
R	matrix defined in Appendix B.
Re	Reynold number
s	spacing defined in Appendix A.
$\hat{S}$	matrix defined in Equation (4).
T	temperature
T_o	stagnation temperature
V	velocity, along η-line defined on page 9.
W	matrix defined in Appendix B.

$\underline{X}$	vector defined in Appendix C.
Y	matrix defined in Appendix B.
a	coefficient in equation (A4) of Appendix A.
a_1	variable defined on page 65.
a_2	variable defined on page 65.
a_3	variable defined on page 65.
a_4	variable defined on page 65.
b	coefficient in Equation (A4) of Appendix A.
c	coefficient in Equation (A4) of Appendix A or speed of sound in page 35.
d	constant in Equation (A4) of Appendix A.
e	internal energy
f	function in Equation (A1) of Appendix A.
f_1	coefficient in Equation (A4) of Appendix A.
f_2	coefficient in Equation (A4) of Appendix A.
g	function in Equation (A1) of Appendix A.
g_1	coefficient in Equation (A4) of Appendix A.
g_2	coefficient in Equation (A4) of Appendix A.
h_1	variable defined in Equation (A12) of Appendix A.
h_2	variable defined in Equation (A12) of Appendix A.
k	thermal conductivity
k_1	constant in turbulence model on page 19.
k_2	constant in turbulence model on page 19.
l	the mixing length in turbulence model in page 19.
o	order of magnitude in difference equation.
p	pressure
p_o	stagnation pressure
p_1	guessed pressure value in Equation (15).

p_2	guessed pressure value in Equation (15).
q	matrix defined in Equation (1).
$\bar{q}$	matrix defined in Equation (2).
$\hat{q}$	matrix defined in Equation (4).
r	radial coordinate
r_o	radius of circular pipe
r_w	radial distance at wall Fig. 17,19
t	time
t'	time in transformed system
u	velocity component in x direction.
u_o	inlet velocity for sample calculation.
$\bar{u}$	average velocity on page 36.
u_{dif}	variable defined on page 20.
v	velocity component in r direction.
w	total velocity defined on page 35.
x	axial coordinate
$\bar{\Gamma}$	Riemann invariant defined on page 35.
Δ	forward difference operator in Equation (6).
∇	backward difference operator in Equation (6) or gradient of a function defined in Appendix A.
κ	positive constant defined in page 27.
α	variable defined in Appendix A.
α_1	variable defined on page 65.
α_2	variable defined on page 65.
α_3	variable defined on page 65.
α_4	variable defined on page 65.
β	variable defined in Appendix A

γ	variable defined in Appendix A or specific heat ratio.
$\bar{\gamma}$	variable in turbulence model on page 19.
δ	Boundary layer thickness
ε_1	dissipation coefficient in Equation (14)
ε_2	dissipation coefficient in Equation (14)
ζ	finite difference scheme selector on page 12.
η	coordinate in transformed plane.
θ	finite difference scheme selector on page 12.
λ	constant defined on page 51.
λ'	constant on page 51.
μ	dynamic viscosity
μ_o	constant in turbulence model on page 19.
μ_t	turbulent viscosity
ν	kinematic viscosity
ξ	coordinate in transformed plane
ρ	density
$\bar{\rho}$	time - average density
σ_p	convergence criterion for wall pressure residual on page 24.
τ_{rr}	shear stress defined on page 6.
τ_w	shear stress at the wall
τ_{xr}	shear stress defined on page 6.
τ_{xx}	shear stress defined on page 6.
τ_{oo}	shear stress defined on page 6.
ϕ	dependent variable in turbulent flow.
$\tilde{\phi}$	mass average quantity on page 7.
$\bar{\phi}$	time average dependent variable in turbulent flow.
ϕ'	fluctuating quantity in turbulent flow.

ϕ''	fluctuating quantity defined on page 7.
ω	vorticity in turbulent model on page 20.

superscript

d	design condition
n	the n-th time step

subscript

exit	exit condition
i	the i-th point in difference scheme
inner	inner region
j	the j-th point in difference scheme
outer	outer region
r	derivative with respect to r
ref	reference
t	derivative with respect to t
t'	derivative with respect to t'
w	wall
x	derivative with respect to x
η	derivative with respect to η
ξ	derivative with respect to ξ
∞	free stream condition

PREFACE

This work was conducted under a grant NAG 3-338 from NASA Lewis Research Center. Mr. Ron Steinke is the current project monitor. Mr. Richard Roelke and Dr. Louis Povinelli were monitors when the project was started. Mr. Harold E. Rohlik, the chief of the turbine branch, provided us with this research opportunity. During the course of this research, we had discussion with Rod Chima, James Schmidt and Leo Donovan, of NASA Lewis Research Center. Their comments were invaluable. Professor William Joe Rae at State University of New York at Buffalo and Professor Gino Moretti at Brooklyn Polytechnic Institute also provided suggestions and encouragements when the progress was slow. Additional funds from the South Carolina Energy R & D Center and computer time provided by Clemson University were significant. All this support made it possible for us to conclude the project.

SUMMARY

An algorithm for laminar and turbulent viscous compressible two-dimensional flows is presented. For the application of precise boundary conditions over an arbitrary body surface, a body-fitted coordinate system is used in the physical plane. A thin-layer approximation of the Navier-Stokes equations is introduced to keep the viscous terms relatively simple. The flow field computation is performed in the transformed plane. A factorized, implicit scheme is used to facilitate the computation. Sample calculations, for Couette flow, developing pipe flow, isolated airfoil, 2-D compressor cascade flow, and segmental compressor blade design are presented. To a certain extent, the effective use of the direct solver depends on the user's skill in setting up the gridwork, the time step size and the choice of the artificial viscosity. The design feature of the algorithm, an iterative scheme to correct an assumed geometry for a specified surface pressure distribution, works well for subsonic flows. A more elaborate correction scheme is required in treating transonic flows where local shock waves may be involved.

VISCOUS COMPRESSIBLE FLOW DIRECT AND INVERSE COMPUTATION WITH ILLUSTRATIONS

1. Introduction

1.1 Background

In the late 1960's, we extended Stanitz's (1) inverse solution method for planar potential flows to axisymmetric flows. Curved-wall diffusers were designed by using the extended method, and they are referred to as Griffith diffusers (2,3). In Griffith diffusers, the measured wall pressure distributions correlate very well with the prescribed distributions. In the early 1980's, we extended the design procedure to include shear flows to design curved-wall diffusers for short ejectors (4). Even though record high thrust augmentation ratios were observed, the diffuser pressure distributions no longer correlated as well as they did in the sixties. The major difference is that in the Griffith diffusers, there is always a distinct potential core flow while in the ejector diffusers, the entire flow field is often dominated by the viscous forces. It is a natural progression that we began to take on the development of an inverse solution method for flows without neglecting viscosity. The momentum equation considered here-in is the Navier-Stokes equation with the thin-layer approximation. The energy equation is also included as one of the governing equations to account for the compressibility of the fluid. In the Reynolds stress terms, both Baldwin-Lomax (5) and Cebeci's (6) turbulence models were considered. The Baldwin-Lomax model was used in the cascade computations and Cebeci's model was used in the pipe flow computations. The NASA Lewis Research Center initially was interested in the possibility of applying this inverse procedure for gas turbine blade redesign. As the algorithm and computer code were being developed, its interest was shifted to the applicability of the code to compressor blade design. Therefore, a compressor blade of known

surface pressure distribution, reported by Schmidt et al (7), was used to verify the algorithm and the code.

1.2 Outline of the Computational Procedure

The computation begins with an assumed geometry. The flow field computation, including pressure distributions over the boundaries, is performed in a transformed plane. The transformation is from a body-fitted coordinate system. Thompson's (8) general coordinate transformation is used in conjunction with Sorenson's (9) method to provide the orthogonality of the grid work at the solid boundaries. An implicit scheme for solving the compressible Navier-Stokes equation was developed, by the utilization of Beam and Warming's (10) scheme. The direct solver used in this report differs from Steger's (11) in that the present procedure allows solutions of axisymmetric flows and planar flows while Steger's is for planar flows only. The method of obtaining the desired geometry of either an axisymmetric flow passage or a blade cascade is achieved by the Secant method (12), and the virtual velocity method (13). These are progressive, iterative procedures. Thompkins and Tong (13) used an iterative method in correcting geometries, for inviscid flows. Modifications and interfacing of the above techniques were required to yield this comparatively complex procedure. In this report, we consider planar flows as sub-cases of axisymmetric flows. In the sub-cases, appropriate terms are deleted from the axisymmetric flow equations. Flags are used in our computing code to direct the computation to either axisymmetric flow or planar flow. The listing of the computer code is given in Ntone's dissertation (14) and will be deposited at Cosmic. Requests for copies of the code can be directed to Cosmic, Computer Software Management and Information Center, Suite 112, Barrow Hall, Athens, GA 30602.

2. Analysis

In this chapter, the form of the Navier-Stokes equations selected for computation will be presented. The numerical algorithm selected for their solution will then be derived. A brief discussion on boundary conditions will be given here and additional details will be provided in the chapter of sample calculations. A brief presentation of Cebeci's and Baldwin-Lomax turbulence models for Reynolds stress calculation will be given. For improving computational stability at high Reynolds numbers, an artificial viscosity was introduced. It will also be discussed in this chapter.

2.1 Governing Equations

For a viscous, compressible axisymmetric flow, the Navier-Stokes equations are written in the vectorial form similar to Peyret and Viviand (15), as

$$\frac{\partial q}{\partial t} + \frac{\partial F}{\partial x} + \frac{\partial G}{\partial r} = \frac{1}{Re}\left(\frac{\partial F_1}{\partial x} + \frac{\partial G_1}{\partial r}\right) + H \qquad (1)$$

where

$$q = r\begin{bmatrix} \rho \\ \rho u \\ \rho v \\ e \end{bmatrix} \qquad F = r\begin{bmatrix} \rho u \\ \rho u^2 + p \\ \rho uv \\ (e+p)u \end{bmatrix} \qquad G = r\begin{bmatrix} \rho v \\ \rho uv \\ \rho v^2 + p \\ (e+P)v \end{bmatrix}$$

$$F_1 = r\begin{bmatrix} 0 \\ \tau_{xx} \\ \tau_{xr} \\ \frac{\gamma\mu}{Pr}\frac{\partial}{\partial x}\left[\frac{e}{\rho} - \frac{1}{2}(u^2+v^2)\right] + u\tau_{xx} + v\tau_{xr} \end{bmatrix}$$

$$G_1 = r\begin{bmatrix} 0 \\ \tau_{xr} \\ \tau_{rr} \\ \frac{\gamma\mu}{Pr}\frac{\partial}{\partial r}\left[\frac{e}{\rho} - \frac{1}{2}(u^2+v^2)\right] + u\tau_{xr} + v\tau_{rr} \end{bmatrix}$$

$$H = \begin{bmatrix} 0 \\ 0 \\ p - \frac{1}{Re}\,\tau_{\theta\theta} \\ 0 \end{bmatrix} .$$

$$\tau_{xx} = \frac{4}{3}\,\mu\frac{\partial u}{\partial x} - \frac{2}{3}\,\frac{\mu}{r}\,\frac{\partial(rv)}{\partial r}$$

$$\tau_{xr} = \mu\left(\frac{\partial u}{\partial r} + \frac{\partial v}{\partial x}\right)$$

$$\tau_{rr} = \frac{4}{3}\,\mu\frac{\partial v}{\partial r} - \frac{2}{3}\mu\left(\frac{\partial u}{\partial x} + \frac{v}{r}\right)$$

$$\tau_{\theta\theta} = \frac{4}{3}\,\mu\frac{v}{r} - \frac{2}{3}\,\mu\left(\frac{\partial u}{\partial x} + \frac{\partial v}{\partial r}\right) .$$

The above equations are written in the physical plane with cylindrical coordinates (x, r, t) for axisymmetric flows, where x denotes the axial coordinate, r the radial coordinate, and t the time. If the multiplication factor r is set equal to one, the $\frac{1}{r}$ terms go to zero, and the $\frac{\partial}{\partial r}$ terms are replaced by $\frac{\partial}{\partial y}$ then the system of equations becomes useful for planar flows. In the above, ρ is the density of the fluid, u and v the velocity components in x and r direction, respectively, e the sum of thermal energy C_vT and the kinetic energy $\frac{\rho}{2}\,(u^2 + v^2)$, p the pressure, γ the ratio of specific heats and μ the viscosity. The equations are non-dimensionalized using reference values of length, velocity, density and viscosity. The Prandtl number Pr is defined by

$$Pr = \frac{\mu_{ref} C_p}{k_{ref}}$$

where C_p is the specific heat at constant pressure, and k_{ref} is a reference thermal conductivity. The Reynolds number, Re, is defined by

$$Re = \left(\frac{\rho u L}{\mu}\right)_{ref}$$

where L, is the reference length. Pressure, p, is obtained from the equation of state

$$p = (\gamma-1)\,[e - 1/2\ \rho(u^2 + v^2)]$$

For laminar flow, the dependence of μ on temperature can be accounted for by using Sutherland's relation:

$$\mu = \left(\frac{T}{T_{ref}}\right)^{3/2} \frac{C_2 + T_{ref}}{C_2 + T} \quad ,$$

where T denotes temperature, and

$$C_2 = 198.6\ ^\circ R$$

For turbulent flows, it is customary to express each dependent variable as the sum of a mean and a fluctuating quantity, such as $\phi = \overline{\phi} + \phi'$, and then time-average the Navier-Stokes equations. For compressible flows, this procedure leads to the presence of second and third order moments of the fluctuating variables due to the density fluctuations. To avoid this, the concept of mass averaging (16-18) is introduced. For example, if ϕ represents the instantaneous value of a dependent variable, then the following decomposition is used:

$$\phi = \tilde{\phi} + \phi''$$

where $\tilde{\phi}$ is a mass averaged quantity, defined as $\tilde{\phi} = \overline{\rho\phi}/\overline{\rho}$, ϕ'' is a fluctuation, and the $\overline{\phi}$ denotes the time averaged quantity. The ϕ'' is then related to ϕ', which is the customary fluctuation quantity, by

$$\phi'' = \frac{\overline{\rho'\phi'}}{\overline{\rho}} \quad .$$

For Navier-Stokes equations, the mass averaged decomposition is applied to u and v while the customary time averaging is applied to ρ, e and p. The time

averaged turbulent Navier-Stokes equations are essentially the same as those for laminar flows, except that one must add to each laminar shear stress and heat flux term its corresponding turbulent contribution resulting from fluctuations. Thus, for turbulent flows, a turbulent viscosity μ_t is added to the molecular viscosity μ, and the coefficient $\frac{\gamma\mu}{Pr}$ is replaced by $\gamma\left(\frac{\mu}{Pr} + \frac{\mu_t}{Pr_t}\right)$, where Pr_t is a turbulent Prandtl number. However, proper closure of the equations is not achieved until a method of calculating the values of μ_t and Pr_t is introduced. This subject will be dealt with in the section on "Turbulence Model."

In many problems, one wishes to have boundary conditions satisfied exactly on an arbitrarily shaped body surface. Therefore, the need for a coordinate transformation from the cartesian coordinate system (x, r, t) to a more general curvilinear system (ξ, η, t') arises. With the coordinate transformation

$$\xi = \xi(x, r, t)$$

$$\eta = \eta(x, r, t)$$

$$t' = t \ ,$$

the axisymmetric Navier-Stokes equations can be rewritten as:

$$\frac{\partial \overline{q}}{\partial t'} + \frac{\partial \overline{F}}{\partial \xi} + \frac{\partial \overline{G}}{\partial \eta} = \frac{1}{Re}\left(\frac{\partial \overline{F}_1}{\partial \xi} + \frac{\partial \overline{G}_1}{\partial \eta}\right) + \overline{H} \ ,$$

where

$$\overline{q} = q/J$$

$$\overline{F} = \xi_t \, \overline{q} + \xi_x \, F/J + \xi_r \, G/J$$

$$\overline{G} = \eta_t \overline{q} + \eta_x F/J + \eta_r G/J$$

$$\overline{G}_1 = \eta_x F_1/J + \eta_r G_1/J$$

$$\overline{H} = H/J$$

$$J = \xi_x \eta_r - \xi_r \eta_x = 1/(x_\xi r_\eta - x_\eta r_\xi)$$

If one introduces the velocities, V, along η = constant line and, U, along ξ = constant line, then $\overline{F}$ and $\overline{G}$ become:

$$\overline{F} = \frac{r}{J} \begin{bmatrix} \rho U \\ \rho u U + \xi_x p \\ \rho v U + \xi_r p \\ (e + p) U - \xi_t p \end{bmatrix}$$

$$\overline{G} = \frac{r}{J} \begin{bmatrix} \rho V \\ \rho u V + \eta_x p \\ \rho v V + \eta_r p \\ (e + p) V - \eta_t p \end{bmatrix} ,$$

where

$$U \equiv \xi_t + u\xi_x + v\xi_r$$

$$V \equiv \eta_t + u\eta_x + v\eta_r \quad .$$

In the above transformed equations, the presence of the matrices ξ_x, ξ_r, η_x, η_r and the Jacobian, J, implies that the coordinate transformation is known. The details of how the transformation was obtained are given in Appendix A. For a stationary boundary, ξ_t and η_t are zero. For a moving boundary ξ_t and η_t must be specified.

The viscous part, (RHS of Equation (2)), contains a large number of terms. These items can be greatly reduced if one uses the "thin layer"

assumption, according to which ξ-derivatives in the viscous part are neglected as small compared to the η-derivative. Such an approximation is different from that of the usual boundary layer equation assumption, in the sense that it allows a pressure gradient across the streamlines even inside the boundary layer. Degani and Steger (19) recently presented a comparison of calculations using the thin layer assumption and the full Navier-Stokes equations to validate the approximation. When the thin layer approximation is incorporated into the governing equations, Equation (2) becomes:

$$\frac{\partial \bar{q}}{\partial t^1} + \frac{\partial \bar{F}}{\partial \xi} + \frac{\partial \bar{G}}{\partial \eta} = \frac{1}{Re} \frac{\partial \bar{G}_1}{\partial \eta} + \bar{H} \tag{3}$$

where

$$\bar{G}_1 = \frac{r}{J} \begin{bmatrix} 0 \\ \mu(\eta_x^2 + \eta_r^2)u_\eta + \frac{1}{3}\mu\eta_x(u_\eta\eta_x + v_\eta\eta_r) - \frac{2}{3}\mu\frac{v}{r}\eta_x \\ \mu(\eta_x^2 + \eta_r^2)v_\eta + \frac{1}{3}\mu\eta_r(u_\eta\eta_x + v_\eta\eta_r) - \frac{2}{3}\mu\frac{v}{r}\eta_r \\ \frac{\gamma\mu}{Pr}\left[\frac{e}{\rho} - \frac{1}{2}(u^2 + v^2)\right]_\eta(\eta_x^2 + \eta_r^2) + \frac{\mu}{2}(\eta_x^2 + \eta_r^2)(u^2 + v^2)_\eta \\ + \frac{\mu}{6}\left[(u^2)_\eta\eta_x^2 + (v^2)_\eta\eta_r^2 + 2(uv)_\eta\eta_x\eta_r\right] - \frac{3}{2}\mu\frac{u}{r}(u\eta_x + v\eta_r) \end{bmatrix}$$

and

$$\bar{H} = \frac{1}{J} \begin{bmatrix} 0 \\ 0 \\ p - \frac{1}{Re}\left[\frac{4}{3}\mu\frac{v}{r} - \frac{2}{3}\mu(u_\eta\eta_x + v_\eta\eta_r)\right] \\ 0 \end{bmatrix}$$

If we let the multiplication factor r be one in Equation (3), 1/r terms be zero, then $\bar{H}$ will vanish, and Equation (4) the governing equation for planar flows will be

$$\frac{\partial \hat{q}}{\partial t'} + \frac{\partial \hat{F}}{\partial \xi} + \frac{\partial \hat{G}}{\partial \eta} = \frac{1}{Re} \frac{\partial \hat{S}}{\partial \eta} \tag{4}$$

where

$$\hat{q} = \bar{q}/r \ , \ \hat{F} = \bar{F}/r \ , \ \hat{G} = \bar{G}/r$$

and

$$\hat{S} = \frac{1}{J} \begin{bmatrix} 0 \\ \mu(\eta_x^2 + \eta_r^2)\, u_\eta + \frac{\mu}{3}\eta_x(\eta_x u_\xi + \eta_r v_\eta) \\ \mu(\eta_x^2 + \eta_r^2)\, v_\eta + \frac{\mu}{3}\eta_r(\eta_r u_\eta + \eta_r v_\eta) \\ \frac{\gamma\mu}{pr}\left[\frac{e}{\rho} - \frac{1}{2}(u^2+v^2)\right]_\eta(\eta_x^2 + \eta_r^2) + \frac{\mu}{2}(\eta_x^2 + \eta_r^2)(u^2+v^2)_\eta \\ + \frac{\mu}{6}\left[(u^2)_\eta \eta_x^2 + (v^2)_\eta \eta_r^2 + 2(uv)_\eta \eta_x \eta_r\right] \end{bmatrix}$$

The axisymmetric equations can also be written in a form very similar to the planar flow governing equations, and is shown as follows:

$$\frac{\partial \hat{q}}{\partial t'} + \frac{\partial \hat{F}}{\partial \xi} + \frac{\partial \hat{G}}{\partial \eta} = \frac{1}{Re} \frac{\partial \hat{G}_1}{\partial \eta} + \hat{H}' \ , \tag{5}$$

where

$$\hat{G}_1 = \bar{G}_1/r$$

$$\hat{H}' = \frac{1}{r}\left(\frac{1}{Re}\hat{G}_1' - \hat{G}'\right)$$

$$\hat{G}' = \frac{1}{J} \begin{bmatrix} \rho v \\ \rho uv \\ \rho v^2 \\ (e+p)v \end{bmatrix}$$

and

$$\hat{G}_1' = \frac{1}{J}\begin{bmatrix} 0 \\ \mu(u_\eta \eta_r + v_\eta \eta_x) \\ 2\mu\left(v_\eta \eta_r - \frac{v}{r}\right) \\ \frac{\gamma\mu}{Pr}\left[\frac{e}{\rho} - \frac{1}{2}(u^2 + v^2)\right]_\eta \eta_r + \mu u (u_\eta \eta_r + v_\eta \eta_x) \\ + \frac{4}{3}\mu v v_\eta \eta_r - \frac{2}{3}\mu v u_\eta \eta_x - \frac{2}{3}\mu \frac{v^2}{r} \end{bmatrix} .$$

In this report examples are presented to show the solutions for Equations (3) and (4). Equation (5) is suited for more complicated geometries than equation 3. However, the computing time will be longer when Equation (5) is used.

2.2 Numerical Schemes

In this section the derivation of the finite difference equations used in the solution of Equation (3) is presented. Following a similar procedure, the corresponding finite difference equations for Equations (4) and (5) were also derived but are not included in this report.

The algorithm selected here is the implicit factored scheme of Beam and Warming. As a starting point, the time differencing formula is written in Pade's form as,

$$\frac{\partial \bar{q}^n}{\partial t'} = \frac{1}{\Delta t'} \frac{(1+\zeta)\Delta - \zeta\Delta}{1+\theta\Delta} \bar{q}^n + (\theta - \zeta + \frac{1}{2})\, 0\,(\Delta t') + 0\,(\Delta t'^2). \qquad (6),$$

where Δ and ∇ are forward and backward difference operators, and superscript "n" represents the nth time step. This is demonstrated by:

$$\Delta \bar{q}^n = \bar{q}^{n+1} - \bar{q}^n$$

$$\nabla \bar{q}^n = \bar{q}^n - \bar{q}^{n-1}$$

and $t' = n(\Delta t')$ with positive integer of n. Recognizing $\Delta\bar{q}^{n-1} = \nabla\bar{q}^{n}$, Equation (6) can be rewritten as

$$\Delta\bar{q}^{n} = \frac{\theta\Delta t'}{1+\zeta}\,\Delta\left(\frac{\partial\bar{q}^{n}}{\partial t'}\right) + \frac{\Delta t'}{1+\zeta}\,\frac{\partial\bar{q}^{n}}{\partial t'} + \frac{\zeta}{1+\zeta}\,\Delta\bar{q}^{n+1}$$

$$+ O\left(\theta - \zeta - \frac{1}{2}\right)(\Delta t'^{2}) + O(\Delta t'^{3}) \; . \qquad (7)$$

Using Equation (3) we can show that Equation (7) takes the following form:

$$\frac{\Delta t'}{1+\zeta}\left[\left(-\frac{\partial\bar{F}}{\partial\zeta} - \frac{\partial\bar{G}}{\partial\eta} + \frac{1}{Re}\,\frac{\partial\bar{G}_{1}}{\partial\eta} + \bar{H}\right)^{n}\right]$$

$$+ \frac{\theta\Delta t'}{1+\zeta}\left[\frac{\partial}{\partial\zeta}\left(-\Delta\bar{F}^{n}\right) + \frac{\partial}{\partial\eta}\left(-\Delta\bar{G}^{n}\right) + \frac{1}{Re}\,\frac{\partial}{\partial\eta}\left(\Delta\bar{G}_{1}^{n}\right) + \Delta\bar{H}^{n}\right]$$

$$= \Delta\bar{q}^{n} - \frac{\zeta}{1+\zeta}\,\Delta\bar{q}^{n-1} + \left(\theta-\zeta-\frac{1}{2}\right) O(\Delta t'^{2}) + O(\Delta t'^{3}). \qquad (8)$$

2.2.1 Linearization

Equation (8) is non-linear because $\Delta\bar{F}^{n}$, $\Delta\bar{G}^{n}$, $\Delta\bar{G}^{n}$, and $\Delta\bar{H}^{n}$ contain terms depending on $\bar{q}^{n+1}$. However, those terms can be linearized, as shown below for $\Delta\bar{F}^{n}$:

$$\bar{F}^{n} = \xi_{t}{}^{n}\bar{q}^{n} + \xi_{x}{}^{n}\,(F(q)/J)^{n} + \xi_{r}{}^{n}\,(G(q)/J)^{n}$$

then

$$\Delta\bar{F}^{n} = \left\{\xi_{t}{}^{n+1}\,\bar{q}^{n+1} + \xi_{x}{}^{n+1}\,(F(q)/J)^{n+1} + \xi_{r}{}^{n+1}(G(q)/J)^{n+1}\right\}$$

$$- \left\{\xi_{t}\bar{q}^{n} + \xi_{x}{}^{n}\,(F(q)/J)^{n} + \xi_{r}{}^{n}\,(G(q)/J)^{n}\right\} \; .$$

From the definitions of F and G, it can be shown that:

$$F(q)/J = F(q/J) = F(\bar{q})$$

$$G(q)/J = G(q/J) = G(\bar{q}),$$

and

$$\frac{\partial}{\partial \bar{q}} F(\bar{q}) = \frac{\partial F(q)}{\partial q} \equiv A$$

$$\frac{\partial}{\partial \bar{q}} G(\bar{q}) = \frac{\partial G(q)}{\partial q} \equiv B.$$

One may also show from matrix multiplication, that

$$F(\bar{q}) = A\bar{q} \quad \text{and} \quad G(\bar{q}) = B\bar{q}.$$

The Jacobian matrices, A and B, are given in Appendix B. Expanding $F(\bar{q})$ in a Taylor series yields:

$$F(\bar{q})^{n+1} = F(\bar{q})^n + \Delta\bar{q}^n \left(\frac{\partial F(\bar{q})}{\partial \bar{q}}\right)^n + \ldots ,$$

and since

$$\Delta\bar{q}^n = \bar{q}^{n+1} - \bar{q}^n = \Delta t\left(\frac{\partial \bar{q}}{\partial t}\right)^n + O(\Delta t^2)$$

then,

$$F(\bar{q})^{n+1} = F(\bar{q})^n + A^n (\bar{q}^{n+1} - \bar{q}^n) + O(\Delta t^2)$$

$$= A^n \bar{q}^{n+1} + O(\Delta t^2)$$

similarly,

$$G(\bar{q})^{n+1} = B^n \bar{q}^{n+1} + O(\Delta t^2)$$

then

$$\Delta\bar{F}^{n+1} = [\xi_t^{n+1} I + \xi_x^{n+1} A^n + \xi_r^{n+1} B^n]\, \Delta\bar{q}^n + (\xi_t^{n+1} - \xi_t^n)\bar{q}^n$$

$$+ (\xi_x^{n+1} - \xi_x^n)\, F(\bar{q})^n + (\xi_r^{n+1} - \xi_r^n)\, G(\bar{q})^n \ .$$

A similar expression for $\Delta\bar{G}^n$ can also be obtained, if ξ is replaced by η. Equation (8) can be now expressed as follows:

$$I + \frac{\theta\Delta t'}{1+\zeta}\left[\frac{\partial}{\partial\xi}(\tilde{A}^n \Delta\bar{q}^n) + \frac{\partial}{\partial\eta}(\tilde{B}^n\Delta\bar{q}^n) - \frac{1}{Re}\frac{\partial}{\partial\eta}(\Delta\bar{G}_1^n) - \Delta\bar{H}^n\right]$$

$$= -\frac{\Delta t'}{1+\zeta}\left[\frac{\partial\tilde{F}^n}{\partial\xi} + \frac{\partial\tilde{G}^n}{\partial\eta} - \frac{1}{Re}\frac{\partial\bar{G}_1^n}{\partial\eta} + \bar{H}^n\right] + \frac{\zeta}{1+\zeta}\Delta\bar{q}^{n-1}$$

$$+ (\theta - \zeta - \tfrac{1}{2})\, O(\Delta t'^2) + O(\Delta t'^3) \ , \qquad (9)$$

where

$$\tilde{A}^n = \xi_t^{n+1} I + \xi_x^{n+1} A^n + \xi_r^{n+1} B^n$$

$$\tilde{B}^n = \eta_t^{n+1} I + \eta_x^{n+1} A^n + \eta_r^{n+1} B^n$$

$$\tilde{F}^n = [(1-\theta)\xi_t^n + \theta\xi_t^{n+1}]\,\bar{q}^n + [(1-\theta)\xi_x^n + \theta\xi_x^{n+1}]\, F^n(\bar{q})$$

$$+ [(1-\theta)\xi_r^n + \theta\,\xi_r^{n+1}]\, G^n(\bar{q})$$

and

$$\tilde{G}^n = [(1-\theta)\eta_t^n + \theta\eta_t^{n+1}]\,\bar{q}^n + [(1-\theta)\eta_x^n + \theta\eta_x^{n+1}]\, F^n(\bar{q})$$

$$+ [(1-\theta)\eta_r^n + \theta\,\eta_r^{n+1}]\, G^n(\bar{q}) \ .$$

In the present research, the three-point backward implicit scheme is used, where $\theta = 1$ and $\zeta = \frac{1}{2}$. In the direct solver, the boundaries are fixed. Therefore, the metrics do not change with respect to time. It can then be shown that

$$\tilde{F}^n = \bar{F}^n \quad \text{and} \quad \tilde{G}^n = \bar{G}^n \ ,$$

and $\tilde{F}^n$ and $\tilde{G}^n$ no longer depend on $(\bar{q})^{n+1}$. One can approximate $\Delta\bar{G}_1{}^n$ in the following form:

$$\Delta\bar{G}_1^n = \left(\frac{r}{J}\bar{M} + \bar{M}_1\right)^n \Delta\bar{q}^n \ ,$$

and, similarly,

$$\Delta\bar{H}^n = (D + E)^n \Delta\bar{q}^n \ .$$

These are linear because $\bar{M}$, $\bar{M}_1$, D and E are expressed at time n, and are therefore known, just as in the case of $\Delta\bar{F}^n$ and $\Delta\bar{G}^n$. The matrices $\bar{M}_1$, $\bar{M}$, D and E are listed in Appendix B. Then the linearized algorithm appears as follows:

$$\left\{I + \frac{\theta\Delta t'}{1+\zeta}\left[\frac{\partial}{\partial\xi}\tilde{A}^n + \frac{\partial}{\partial\eta}\tilde{B}^n - \frac{1}{Re}\frac{\partial}{\partial\eta}\left(\frac{r}{J}\bar{M} + \bar{M}_1\right)^n - D^n - E^n\right]\right\}\Delta\bar{q}^n$$

$$= \frac{\Delta t'}{1+\zeta}\left[-\frac{\partial\tilde{F}^n}{\partial\xi} - \frac{\partial\tilde{G}^n}{\partial\eta} + \frac{1}{Re}\frac{\partial\bar{G}_1}{\partial\eta} + \bar{H}^n\right] + \frac{\zeta}{1+\zeta}\Delta\bar{q}^{n-1} + O(\theta-\zeta-\tfrac{1}{2})O(\Delta t'^2) + O(\Delta t'^3). \tag{10}$$

2.2.2 Factorization

A major gain in computational efficiency may result if Equation (9) is written in the following factored form:

$$\left[I + \frac{\theta\Delta t'}{1+\zeta}\frac{\partial}{\partial\xi}\tilde{A}^n\right]\left[I + \frac{\theta\Delta t'}{1+\zeta}\left(\frac{\partial}{\partial\eta}\tilde{B}^n - \frac{1}{Re}\frac{\partial}{\partial\eta}\left(\frac{r}{J}\bar{M} + \bar{M}_1\right)^n - D^n - E^n\right]\Delta\bar{q}^n$$

$$= \text{R.H.S. of equation (10).}$$

and

$$\bar{q}^{n+1} = \bar{q}^{n} + \Delta\bar{q}^{n} .$$

Equation (11), the factored equation, differs from Equation (10) only by terms which do not affect the stated accuracy. Using Equation (11), the two-dimensional operator of Equation (10) was reduced to two one-dimensional operators.

For spatial discretization, the central difference scheme is used, and the terms $(\frac{\partial\phi}{\partial\xi})_{i,j}$ and $\frac{\partial}{\partial\eta}(\beta\frac{\partial\phi}{\partial\eta})_{i,j}$ are represented by the following approximations:

$$\frac{\partial\phi}{\partial\xi})_{i,j} = \frac{\phi_{i+1,j} - \phi_{i-1,j}}{2\Delta\xi} + O(\Delta\xi^2)$$

and

$$\frac{\partial}{\partial\eta}(\beta\frac{\partial\phi}{\partial\eta})_{i,j} = \frac{(\beta_{i+1,j} + \beta_{i,j})(\phi_{i,j+1} - \phi_{i,j}) - (\beta_{i,j} + \beta_{i,j-1})(\phi_{i,j} - \phi_{i,j-1})}{2(\Delta\eta)^2}$$

$$+ O(\Delta\eta^2),$$

When $\Delta\xi$ and $\Delta\eta$ are taken to be 1, Equation (11) becomes:

$$L_{i-1}\Delta\bar{q}^{*}_{i-1,j} + Q_i\,\Delta\bar{q}^{*}_{i,j} + N_{i+1}\Delta\bar{q}^{*}_{i+1,j} = K_{i,j} \qquad (12)$$

where

$$L_{i-1} = \frac{1}{2}\frac{\theta(\Delta t')}{1+\zeta}\,\tilde{A}^{n}_{i-1,j}$$

$$Q_i = I$$

$$N_{i+1} = \frac{1}{2}\frac{\theta(\Delta t')}{1+\zeta}\,\tilde{A}^{n}_{i-1,j}$$

and

$$2 \leq i \leq i_{max} - 1.$$

The K_{ij} represents the right hand side of Equation (10), and L_{i-1}, Q_i, N_{i+1} are 4x4 matrices. The solution of Equation (12) for $\Delta\bar{q}^*_{i,j}$ requires the inversion of a block tridiagonal matrix. This procedure is shown in Appendix C. The solution of Δq's, of Equation (11), which is referred to as the η-sweep, is obtained from the following:

$$L_{j-1}\,\Delta\bar{q}^n_{i,j-1} + Q_j\,\Delta\bar{q}^n_{i,j} + N_{j-1}\Delta\bar{q}^n_{i,j+1} = \Delta\bar{q}^{*n}_{i,j}, \tag{13}$$

where

$$L_{j-1} = \frac{\theta\Delta t'}{1+\zeta}\left(-\tilde{B}^n_{i,j-1} - \frac{1}{Re}W^n_{i,j-1} + \frac{1}{Re}\bar{M}1^n_{i,j-1} - E^n_{i,j-1}\right)$$

$$N_{j+1} = \frac{\theta\Delta t'}{1+\zeta}\left(\tilde{B}^n_{i,j+1} - \frac{1}{Re}Y^n_{i,j+1} - \frac{1}{Re}\bar{M}1^n_{i,j+1} - E^n_{i,j+1}\right)$$

$$Q_j = I - \frac{\theta\Delta t'}{1+\zeta}\left(\frac{1}{Re}R^n_{i,j} + 2D^n_{i,j}\right)$$

and

$$2 \leq j \leq j_{max} - 1.$$

The matrices W, Y, R are given in Appendix B. For each time step, the solution of the previous time step is used to calculate the R.H.S. of Equation (10) and the L.H.S. of Equations (12) and (13). The solutions of Equations (12), (13) and (11a) yield the flow field at interior points of the new time step. At the boundaries, either the flow variables are specified, or they are calculated from the known values at the interior points. To initiate the calculation, an initial set of values must be assumed. The three-point backward scheme uses three time levels; the third level is calculated from the previous two levels. Therefore, one could not start the calculation with just an initial solution at n=0. The trapezoidal

rule is employed for the first time iteration, and the three-point backward scheme is used thereafter.

2.3. Boundary Conditions

The importance of treating the boundary conditions correctly has long been pointed out by authors such as Moretti (20). The 1981 Symposium on Numerical Boundary Condition Procedures (21) was a recognition of the importance of this aspect in numerical computations. Essentially, boundary conditions affect both the well-posedness of initial-boundary value problems and the stability of their numerical solution (22).

At in-flow either the velocity components and the density (or temperature) or the stagnation temperature and pressure and the flow angle were specified. At solid boundaries, both u and v are zero and either a constant surface temperature or an adiabatic wall condition is specified. Fluid properties which are not specified at boundaries are obtained from solutions at interior points by extrapolation. At the outflow boundary, where p is specified, ρ, u and v are obtained by linear extrapolation. Details on the extrapolation are provided in Appendix D.

2.4 Turbulence Model

As stated earlier, a complete closure of the governing equations require that a turbulence model be provided. In this research, two turbulence models, namely Cebeci's algebraic model and the variation of it introduced by Baldwin and Lomax (5), were examined.

Cebeci's model (6) is a two-layer model in which the calculation of the eddy viscosity, μ_t, depends on whether one considers points in the inner region or the outer region. In the inner region, the expression for μ_t is based on Prandtl's mixing length theory:

$$(\mu_t)_{inner} = \rho \ell^2 \left| \frac{\partial u}{\partial y} \right| ,$$

where y is the normal distance from the wall and ℓ the mixing length. They are obtained from the Van Driest expression

$$\ell = k_1 y \left[1-\exp\left(\frac{-y}{A^+}\right)\right] ,$$

with

$$k_1 = 0.4$$

$$A^+ = 26\nu \left(\frac{\tau_w}{\rho_w}\right)^{-1/2} .$$

Here, ν is the kinematic viscosity, and τ_w and ρ_w are the shear stress and density at the wall, respectively.

In the outer region, μ_t is calculated from:

$$(\mu_t)_{outer} = \mu_o c_{kleb} \rho$$

where

$$\mu_o = k_2 \int_o^\infty (u_e - u) dy ,$$

and

$$c_{kleb} = \left[1+5.5\left(\frac{y}{\delta}\right)^6\right]^{-1} .$$

In the above, u_e is the velocity at the edge of the boundary layer, δ is the boundary layer thickness, γ is the Klebanoff intermittency factor, and k_2 = 0.0168.

The inner region extends from the wall to the crossover point y_c, where $(\mu_t)_{inner} = \mu_o$. For $y > y_c$, values of $(\mu_t)_{outer}$ are applicable. One of the difficulties in applying Cebeci's model lies in the accurate determination of δ. Baldwin and Lomax (25) pointed out that significant errors would result

from the inaccurate evaluation of δ and modified Cebeci's model to avoid this calculation.

In the Baldwin and Lomax model, the eddy viscosity for the inner region is obtained from:

$$(\mu_t)_{inner} = \rho \, \ell^2 \, |\omega| ,$$

where

$$w = \frac{\partial u}{\partial r} - \frac{\partial v}{\partial x} .$$

For the outer region, the following formula is used

$$(\mu_t)_{outer} = k_2 \, C_{cp} \, \rho \, F_{wake} \, F_{kleb}(y) ,$$

where

$$C_{cp} = 1.6$$

$$F_{wake} = \left\{ \begin{array}{l} y_{max} \, F_{max} \text{ or} \\ C_{wk} \, y_{max} \, U^2_{dif} / F_{max} \end{array} \right\} \quad \text{use the smaller of the two.}$$

$$F_{kleb}(y) = [1+5.5 \, (C_{kleb} \, y/y_{max})^6]^{-1}$$

$$C_{kleb} = 0.3 \quad C_{wk} = 0.25$$

F_{max} is the maximun of F(y) defined as

$$F(y) = \frac{1}{R_1} |\omega| \ell ,$$

and y_{max} is the y-location where F(y) maximum occurs. u_{dif} is given by

$$u_{dif} = (\sqrt{u^2 + v^2})_{max}$$

The success of this model relies on the existence of a well-defined peak for the function F(y) and not having to calculate the boundary layer

thickness, δ. In the current cascade computation, the Baldwin-Lomax model was used in the computer program. No difficulty was encountered.

2.5 Artificial Viscosity

The algorithm described in section 2.2 works well for low Reynolds number calculations, but often requires additional damping terms for computational stability at high Reynolds number. The form of the damping terms used here is the same as Steger's (11). When these damping terms are added, Equation (11) becomes:

$$\left[I + \frac{\theta\Delta t'}{1+\zeta}\frac{\partial}{\partial\zeta}\tilde{A}^n - rJ^{-1}\varepsilon_2\frac{\theta\Delta t'}{1+\zeta}\nabla_\xi\Delta_\xi\frac{J}{r}\right] X$$

$$\left\{I + \frac{\theta\Delta t'}{1+\zeta}\left[\frac{\partial}{\partial\eta}\tilde{B}^n - \frac{1}{Re}\frac{\partial}{\partial\eta}\left(\frac{r}{J}\overline{M} + \overline{M}_1\right)^n - D^n - E^n\right]\right.$$

$$\left. - r\,J^{-1}\,\varepsilon_2\frac{\theta\Delta t'}{1+\zeta}\nabla_\eta\Delta_\eta\frac{J}{r}\right\}\Delta\overline{q}^n$$

$$= \frac{\Delta t'}{1+\zeta}\left[-\frac{\partial\tilde{F}^n}{\partial\xi} - \frac{\partial\tilde{G}^n}{\partial\eta} + \frac{1}{Re}\frac{\partial\overline{G}_1^n}{\partial\eta} + \overline{H}^n\right]$$

$$+ \frac{\zeta}{1+\zeta}\Delta\overline{q}^{n-1} - \varepsilon_1\frac{\theta\Delta t'}{1+\zeta}\,r\,J^{-1}\left[(\nabla_\xi\Delta_\xi)^2 + (\nabla_\eta\Delta_\eta)^2\right]\frac{J}{r}\overline{q}^n \qquad (14)$$

In Equation (14), a fourth order dissipation term has been added to the right hand side of the equation, while second order terms are added to both implicit factors. Operators such as $\nabla\xi$ and $\Delta\xi$ are backward and forward operators. In a central difference approximation,

$$\nabla_\xi\Delta_\xi\phi = \phi_{i+1,j} - 2\phi_{i,j} + \phi_{i-1,j}$$

and

$$(\nabla_\xi\Delta_\xi)^2\phi = \phi_{i+2,j} - 4\phi_{i+1,j} + 6\phi_{i,j} - 4\phi_{i-1,j} + \phi_{i-2,j}$$

are used for second and fourth order derivatives, respectively. The coefficients, ε_1 and ε_2, are dissipation coefficients.

Artificial viscosity terms of this nature were studied by Desideri et al. (22). Their study was based on simplified forms of the governing equations and certain types of boundary conditions. Nevertheless, their limits for the ratio of ε_2 to ε_1 are used as a guideline for the stability behavior of the present damped algorithm.

2.6 Inverse Design

The inverse design consists of computing a wall geometry that satisfies a specified pressure distribution. One may initiate the inverse design with an educated guess-geometry and a reliable procedure for wall modification. Each newly selected wall geometry should yield a wall pressure closer to the target pressure than the previous ones. In this research, two methods have been examined. One is an adaptation of the so-called secant method, often used in the numerical solution of non-linear equations. The other is based on the virtual wall velocity idea previously used by Thompkins and Tong (13).

2.6.1 Secant Method

The secant method is illustrated in the following sketch. In this figure, it is desired to find the zero of a function of $\phi(x)$.

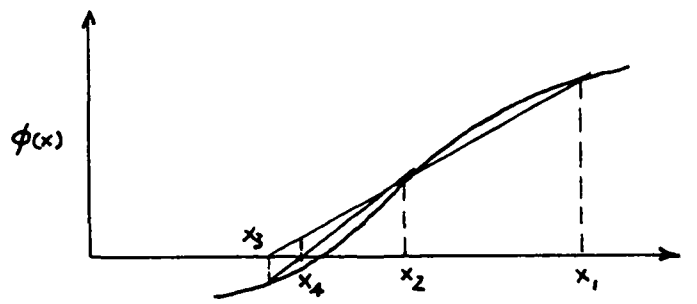

Starting from two initial guesses (x_1,ϕ_1) and (x_2,ϕ_2) on the curve, a straight line is drawn through those two points, intersecting the x-axis at

x_3. Then another straight line is drawn through (x_2,ϕ_2) and (x_3,ϕ_3), intersecting the x-axis at x_4. If this process is continued, the intersection of each new straight line with the x-axis should get closer and closer to the correct value of x for which ϕ vanishes. If the two initial guesses are sufficiently good and the function ϕ sufficiently well-behaved, convergence of the method is quite rapid.

For the extension of the method to inverse design problems, the following formula is used:

$$r = r_1 + \frac{p_d - p_1}{p_2 - p_1} (r_2 - r_1) \tag{15}$$

In Equation (15), all quantities are evaluated at the wall. Subscripts "1" and "2" denote the two guesses used to calculate the next wall geometry and subscript "d" the design pressure. At each wall correction, Equation (15) must be used at every wall point in the region of interest. Clearly, this means smooth wall geometries will be obtained only if wall pressures are smooth. Since this may not necessarily be so, a wall geometry smoothing method must be introduced. In this case, all calculated wall geometries were smoothed by a least squares method, using a low degree polynomial.

In order to apply the above wall correction scheme to a design problem using the thin layer Navier-Stokes equations, it is possible to perform a complete direct calculation on each of the two geometries used to obtain the next one and repeat the process until a satisfactory geometry is obtained. However, it seems computationally more efficient to treat the whole problem as a single direct computation in which wall corrections will be made after a specified number of iterations (time steps) of the direct solver. One may start the calculations using one guess for the geometry. The direct calculations are stopped when the maximum absolute difference between the

current wall pressure and the wall pressure at the previous time step (wall pressure residual) becomes smaller than a specified value σ_p. At this point, the second guess-geometry is used, and direct calculations proceed with this second geometry until the wall pressure residual falls below σ_p. Then using the previous two geometries and their corresponding pressures, a new or the third geometry is calculated using equation (15). This geometry and one of the two guess-geometries whichever has a pressure closer to the design value are used to obtain the 4th geometry. The process repeats with 3rd and 4th geometries as the first and second guess geometries. For accuracy, a small value of σ_p should be specified. However, since σ_p determines the number of direct solver iterations between two wall corrections, the σ_p value may be increased to speed up the computation. For a given σ_p, the number of direct solver iterations decreases as one approaches the target geometry. Therefore, to maintain accuracy, one may decrease σ_p as the target geometry is approached.

The form of Equation (15) makes it suitable for the design of flow passages such as nozzles, diffusers, etc. where the inlet radius is specified and remains fixed throughout the calculations. However, at the exit, where pressure is usually specified, the term P_2-P_1 vanishes, which makes the formula inapplicable. This inconsistency affects points in the neighborhood of the exit, which must be obtained by extrapolation. Here, the extrapolation was done so that the flow can be made nearly parallel at the exit by maintaining the exit wall radius equal to the wall radius of the adjacent point. This, of course, imposes a limitation on the kinds of exit flows to be considered, but there does not seem to be a general rule of extrapolation for the exit wall nodal points.

Due to the presence of $P_2 - P_1$ in the denominator in Equation (15), it is clear that numerical problems will arise if the difference between calculated and target pressures becomes very small. Therefore, calculations must be stopped when that difference becomes smaller than a pre-determined value. Also, initial guesses must be selected such that their corresponding pressure distribution curves do not cross each other.

2.6.2 Virtual Wall Velocity Method

Referring to the flux vector, $\overline{G}$, at the right hand side of Equation (10) and imposing the no-slip condition at the wall, it can be shown that:

$$\overline{G}_w = \left(\frac{r}{J} \begin{bmatrix} 0 \\ \eta_x p \\ \eta_r p \\ 0 \end{bmatrix} \right)_w$$

at all times for the direct calculations (for a fixed wall). The subscript, w, refers to the location at the wall. However, it is possible to imagine a problem where the wall would be moving towards a steady state position corresponding to the target (design) pressure. At that steady state position, $\overline{G}_w$ would be:

$$\overline{G}^d_w = \left(\frac{r}{J} \begin{bmatrix} 0 \\ \eta_x p \\ \eta_r p \\ 0 \end{bmatrix} \right)^d_w$$

where superscript "d" denotes the design conditions. Assuming that the wall moves with a finite velocity towards its steady state position, u, v, V and η_t are no longer zero at the wall. They can be calculated by requiring $\overline{G}_w$ for the moving wall to be equal to $\overline{G}^d_w$, which leads to:

$$\left(\frac{r}{J} \begin{bmatrix} \rho V \\ \rho u V + \eta_x p \\ \rho v V + \eta_r p \\ (e+p)V - \eta_t p \end{bmatrix} \right)_w = \left(\frac{r}{J} \begin{bmatrix} 0 \\ \eta_x p \\ \eta_r p \\ 0 \end{bmatrix} \right)_w^d$$

Equation (16) represents a system of four equations. The first equation is automatically satisfied when the steady state is reached. If geometric changes in time are disregarded, the last equation yields:

$$\eta_t = \left(\frac{e}{p} + 1\right) V,$$

and the second and third equations yield:

$$u = v \frac{\eta_x}{\eta_r} \quad .$$

One may then obtain v from the second equation as:

$$v = \pm \left(\frac{\eta_x^2}{\eta_x^2 + \eta_r^2} \cdot \frac{1}{\rho} | p^d - p | \right)^{1/2} .$$

Now from the equation for η_t and the definition of V, it can be shown that

$$V = - \frac{p}{e} (u\eta_x + v\eta_r) .$$

By applying the rules of partial differentiation, one can show that:

$$\eta_t = -\eta_x x_{t'} - \eta_r r_{t'} .$$

Assuming that the wall only moves in the r-direction, then

$$\eta_t = - \eta_r r_{t'} ,$$

and the magnitude of the wall correction is given by:

$$| \Delta r | = \Delta t' \left(\frac{p}{e} + 1\right) \left(\left(\frac{\eta_x^2}{\eta_r^2} + 1 \right) \left| \frac{p^d - p}{\rho} \right| \right)^{1/2} . \qquad (17)$$

If the calculations are initiated with an assumed geometry, Equation (17) can be used to correct the wall at each time step. However, since this would require the calculation of a new grid at each time step, it is useful to introduce σ_p as described in 2.6.1 to set the number of time steps between two wall corrections. In practice, it may be necessary to multiply the right hand side of Equation (17) by a constant λ. The value of λ should be selected small enough to keep the calculation stable. A value of 0.05 made the computations very slow and a value of 0.2 was satisfactory. Also, the computed r's at the wall are smoothed out by adding to the newly computed r's the expression:

$$\kappa \left(r_{i+1,1} - 2\, r_{i,1} + r_{i-1,1}\right) \quad ,$$

where j=1 denotes the wall, and κ a positive constant. In the calculations performed here, $\kappa = 0.2$ was used.

3. Results and Discussion

In this chapter, some of the cases used to test the algorithm of the numerical solution described in the analysis chapter are presented. Since the inverse design feature of the computational program relies entirely on the direct solution, it is important to assess the capabilities and weaknesses of the direct solver. Therefore, a great part of the chapter will be devoted to the results of the direct solver. Then illustrations will be provided for the inverse design procedure. These illustrative cases have either known analytical or numerical solutions or experimental data. All calculations were performed on an IBM 3081.

3.1 Direct Solution Results

3.1.1 Laminar Flows

3.1.1.1. Flow Formation in Couette Motion

The first case is the two-dimensional flow between two parallel plates at low Reynolds number. One of the plates is held fixed and the other one is suddenly set into motion with a constant velocity, u_o, at a Reynolds number $\frac{u_o H}{\nu}$ of 6.2. Such a flow was considered by Beam and Warming (23), when they extended their algorithm, originally derived for hyperbolic systems in conservation law form, to the Navier-Stokes equations. However, their governing equations were the full Navier Stokes equations in physical coordinates, while a coordinate transformation and a thin-layer approximation are used here.

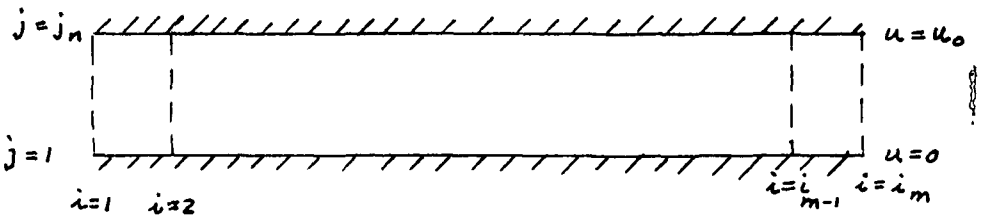

Figure 1: Flow formation in Couette motion

The geometry of the problem is shown in Figure 1. The no-slip condition is applied at the walls (j=1, and $J=j_n$) along with an adiabatic wall condition. At the ξ-boundaries ($\imath=1$ and $\imath=i_m$), periodic boundary conditions are imposed as follows:

$$q_{1,J} = q_{1_m-1,J}$$

$$q_{2,j} = q_{1_m,J}$$

Essentially, the periodic boundary conditions are used here to maintain the non-dependence of the flow field on the x-direction (or ξ-direction). The solution of Equation (4) for this case is compared to the exact solution (24) in Figure 2. The selected grid was uniform and had 6 points in the ξ-direction and 11 points in the η-direction. As expected, the solution showed no variations in the x-direction, and only one x-station needed to be considered. Due to the use of a relatively large time step, only 40 iterations were required for convergence. Because of a large time step, the computed results of 5 and 10 iterations, labeled as 5n and 10n in Figure 2, are in poor agreement with the exact transient solution, while the exact steady state solution and the computed result labeled 40n are in good agreement. This is an indication that the steady state solution is independent of the time step and of the initial conditions. Better

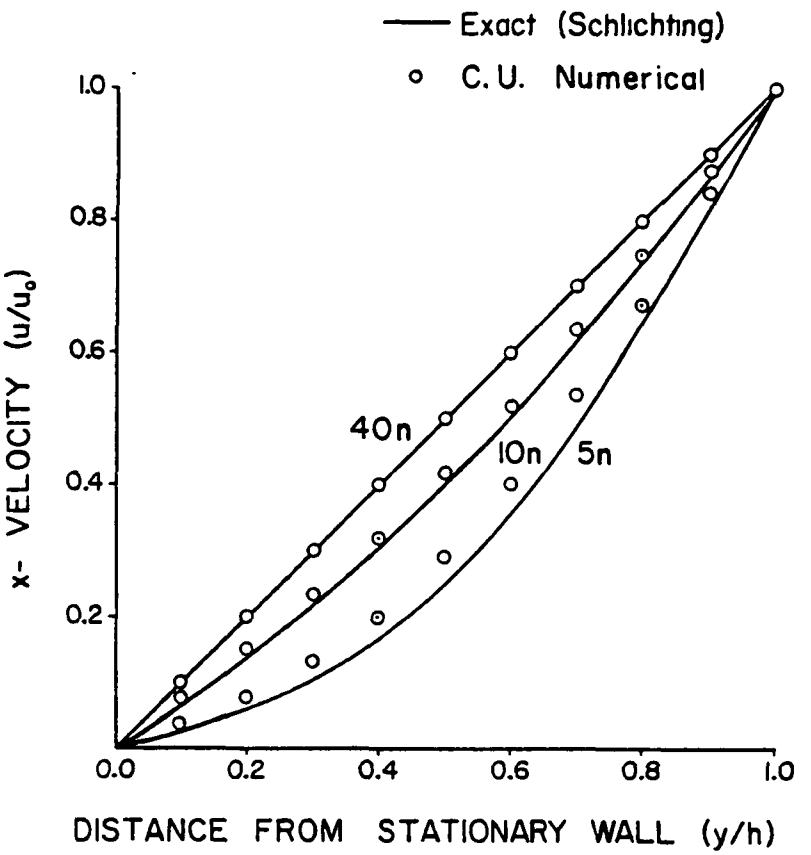

Figure 2. Flow formation in Couette motion.

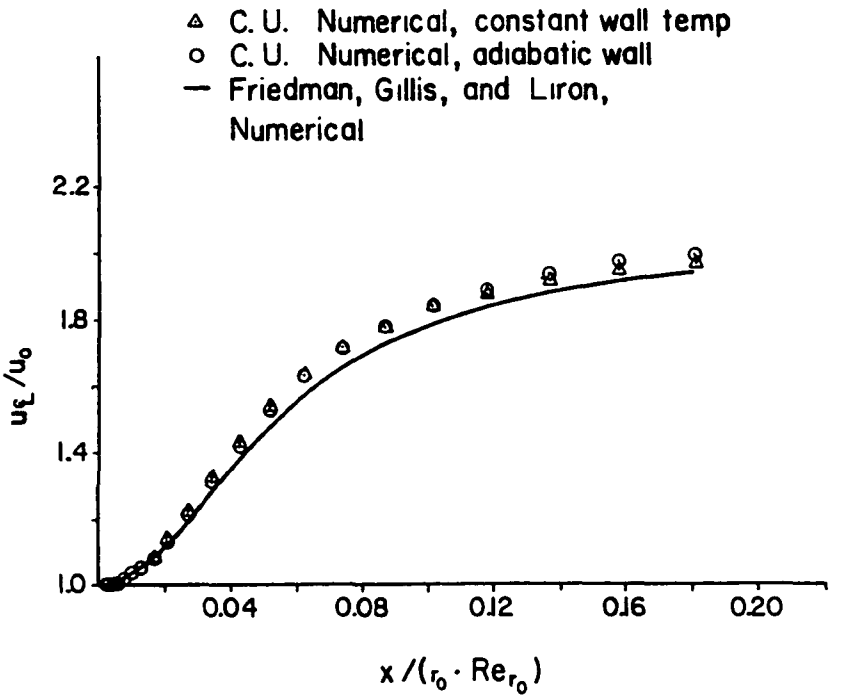

Figure 3. Centerline velocity for the entry region of a pipe at Re_d=40.

agreement with the exact transient solution is obtained with smaller time steps, but more iterations are required.

3.1.1.2. Entry region of a circular pipe at $Re_d = 40$

The second case is the entry region of a circular pipe at low Reynolds number, with a uniform velocity u_o of 100 ft/sec prescribed at the inlet. Friedman et al. (25) used a numerical solution of the incompressible Navier-Stokes equations to show how the Reynolds number affects the flow. In Figure 3, the present solution of the centerline velocity is compared to theirs for a Reynolds number of 40. The present solution (Eq. 3) was obtained with a 21x15 grid and converged in 400 iterations from an impulsive start from uniform conditions. Both a constant temperature wall and an adiabatic wall were considered. It is seen that the constant temperature condition yields a better agreement with Friedman et al.'s solution.

3.1.1.3. Entry region of a circular pipe at $Re_d = 3000$

The third case is the laminar flow in the entrance of a pipe at Re_d = 3000. The uniform velocity prescribed at the inlet was again 100 ft/sec. Because the entry region at this Reynolds number is quite long (above 300 radii), only part of it was considered in the present calculations. A 41x18 grid was used, and the solution converged in 1200 iterations from an impulsive start at uniform conditions. The solution is shown in Figure 4, along with Nikuradse's experimental curves (26) and the analytical results of Campbell and Slattery (27). Also shown is the only point from Reshotko's experimental data, as presented in Reference 27, that falls within the range considered here. Figure 4 shows that the agreement of the present solution with the solution by Campbell and Slattery (27) is generally good, except at the centerline. Nikuradse's data are also presented for comparison. The validity of these data for comparison in this problem, however, has been

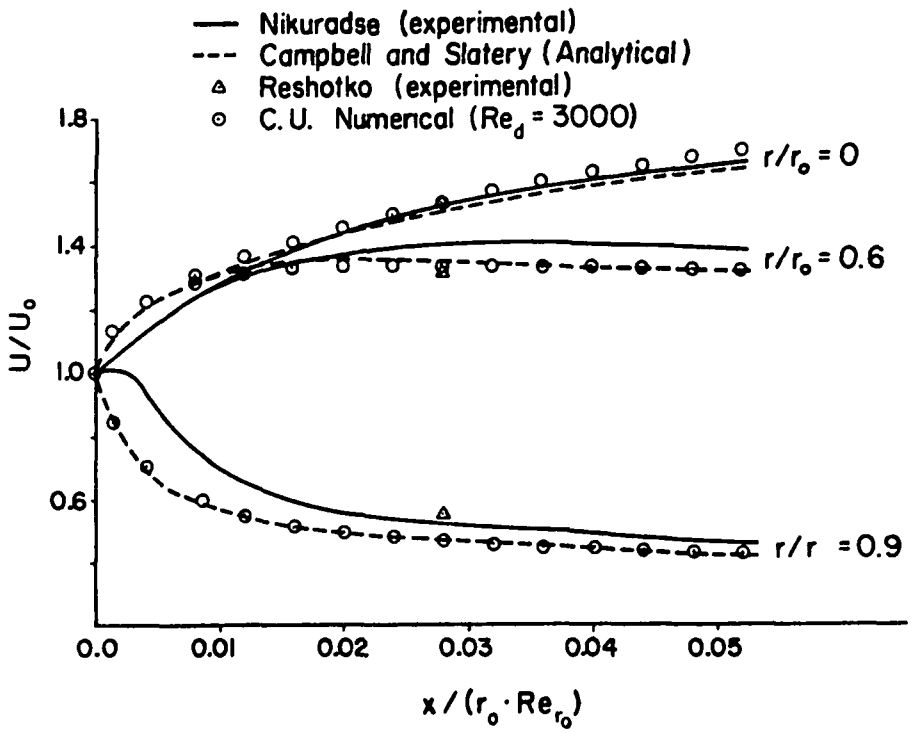

Figure 4. Entry region of a circular pipe. Laminar flow velocity distributions.

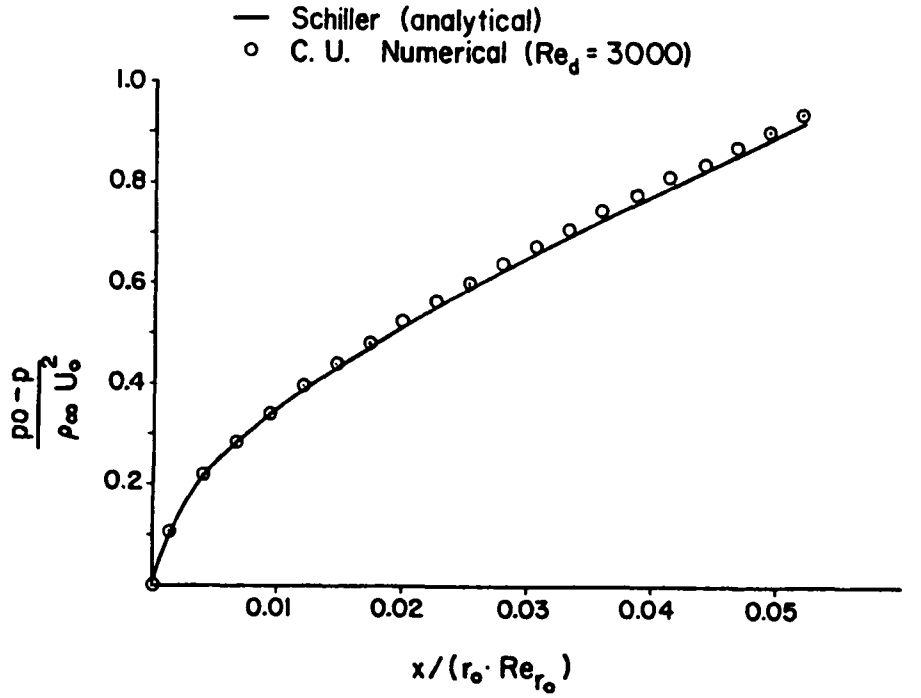

Figure 5. Entry region of a circular pipe. Laminar flow pressure distribution.

questioned by Campbell and Slattery, Shapiro (see discussion in Reference 27) and Sparrow et al. (28). The data point from Reshotko's experiment seems in good agreement with the present solution near the centerline. Figure 5 shows a comparison of the computed non-dimensional present pressure distribution versus the non-dimensional axial distance divided by the Reynolds number with the analytical results of Schiller reported by Tietjens (26), are in very good agreement with experimental data. It should be noted that the present results were obtained using Equation (3) and a rather coarse grid with the spacing in the x-direction taken as one diameter. For pipe flow problems, the solution of Equation (3) at high Reynolds numbers seems to allow such large spacings. However, making Δx much larger than one diameter would result in a computationally unstable situation.

3.1.1.4. Isolated airfoil

As a test of the algorithm for more complicated geometries, the laminar flow over an isolated NACA 0012 airfoil was examined. The calculations were performed at a Reynolds number of 10,000 with respect to the chord length and a free stream Mach number of 0.2. The grid around the airfoil was obtained using Sorenson's code (9) which allows specification of a uniform η-spacing and near-orthogonality at the wall. For the computations, a 79x34 grid of the C-type, as shown in Figure 6, was used. The distance between the wall and the nearest ξ-line was approximately 0.0011, and an elliptic shape outer boundary was specified at 7 chords away from the airfoil. A zero-degree incidence angle (measured from the x-axis) was selected, which means symmetry of the flow field existed about the x-axis. For a geometry such as shown in Figure 6, the elliptic outer boundary is the inflow boundary, while the vertical line at the right is the outflow boundary. At the outflow boundary, the pressure was specified, while ρ, u and v were extrapolated. The

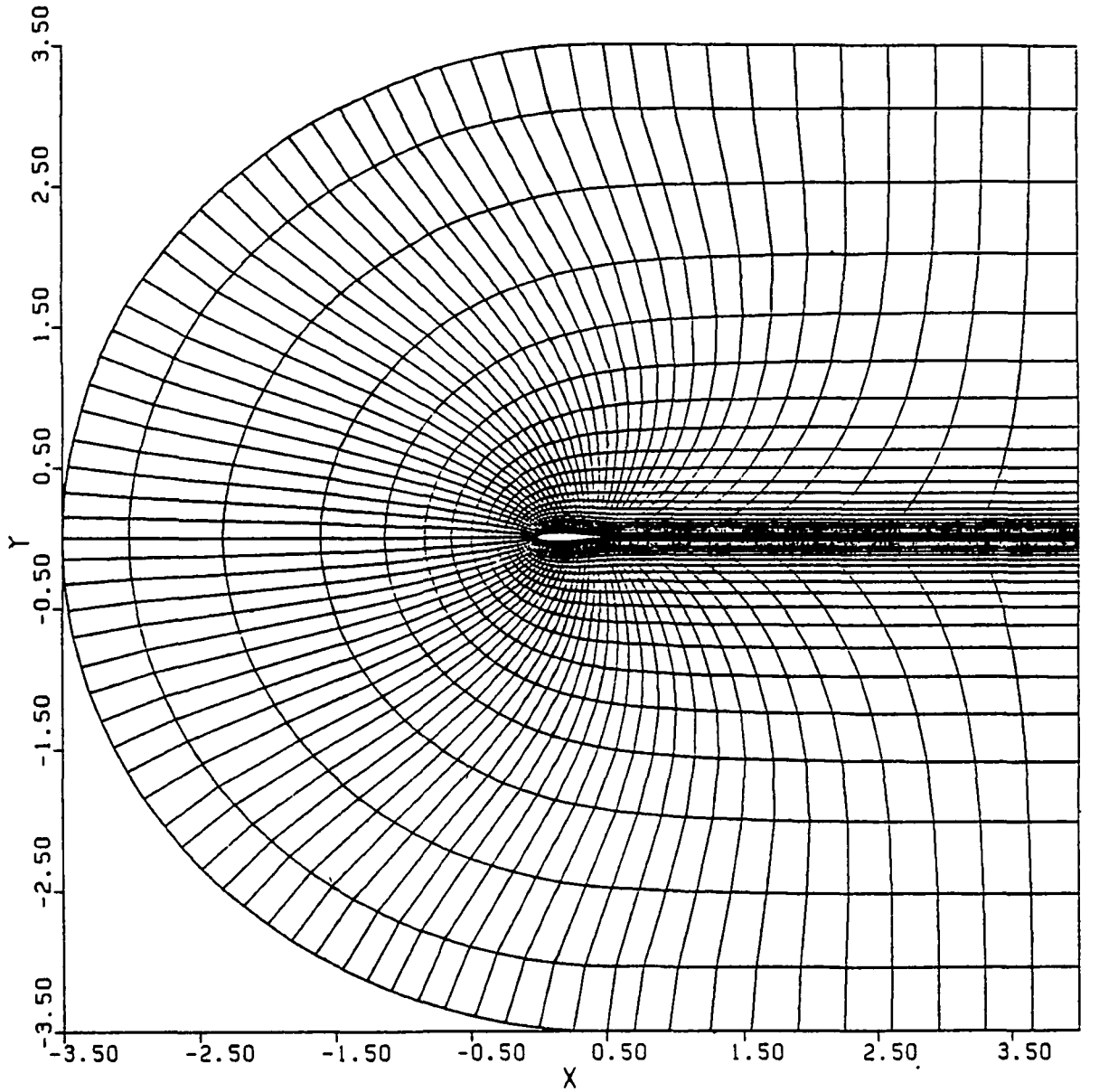

Figure 6. Body-fitted coordinates, NACA 0012 airfoil.

extrapolation was done by taking $\partial/\partial n$ as zero, where n is the direction normal to the outflow boundary. This involves the inversion of three scalar tridiagonal matrices to obtain ρ, u and v at the boundaries. At the inflow boundary, two methods of specifying the boundary conditions were considered. The first consisted in specifying ρ, u and v and extrapolating for P by taking $\frac{\partial P}{\partial \eta} = 0$. The second consisted of specifying the stagnation pressure P_o, and temperature, T_o, and the flow inlet angle, then the left running Riemann invariant, given by:

$$r^- = \omega - \frac{2c}{\gamma-1} \quad ,$$

where c is the speed of sound and ω the total velocity ($\omega = \sqrt{u^2+v^2}$), was linearly extrapolated from the interior to the boundary (see Reference 29). For adiabatic flows, ω at the inlet can be obtained from:

$$\omega = \frac{(\gamma-1)\ r^- + (4(\gamma+1)CpTo - 2(\gamma-1)(r^-)^2)^{1/2}}{(\gamma+1)} \quad ,$$

where all quantities are evaluated at the inlet. Then u and v are obtained from w using trigonometric relations and the flow inlet angle. Also, knowing w and T_o, the inlet static temperature and speed of sound are obtained. The inlet Mach number can then be calculated, and the inlet pressure is obtained from an isentropic relation between P_o and the Mach number. This method is valid for inviscid flows and only approximately correct for viscous flows. Therefore, the inlet boundary should be taken far enough from the airfoil. For the isolated airfoil problem, both methods of treatment of the inflow boundary were found adequate.

At the wall, the no-slip condition (u=v=0) was specified, along with an adiabatic wall condition. The wall pressure was obtained from the interior pressure, which requires the inversion of a scalar tridiagonal matrix. At

the common boundary in the wake region, all flow variables were extrapolated and the averages of the extrapolates from above and below were used. The extrapolation procedure, again, assumed no gradients in the normal direction.

The results of this calculation are shown in Figure 7, where the computed pressure distribution is compared to Mehta's incompressible solution as presented in reference 11. The present solution, obtained after 500 iterations from an impulsive start from free stream conditions, agrees well with Mehta's solution.

3.1.2 Turbulent flows

3.1.2.1. Flow in a circular pipe

In order to assess the validity of the turbulence models presented in Chapter 2, a turbulent flow in a pipe was considered. Calculations were performed in a pipe section 5 radii long. A logarithmic velocity profile was prescribed at the inlet to simulate fully-developed conditions, and the objective of the test was to verify that such a profile would be maintained 5 radii downstream. This test was performed at a Reynolds number, $\frac{\bar{u}D}{\nu}$, of 110,000, with an average velocity , $\bar{u}$, of 100 ft/sec. Both the Cebeci and the Baldwin-Lomax models were examined, and the velocity profiles obtained at the pipe exit using both models are compared to the logarithmic profile in Figure 8. A better agreement with the logarithmic profile is obtained with Cebeci's model. It was also observed from the computed data that the Baldwin-Lomax model tended to underpredict the wall shear. For that reason, Cebeci's model was used in pipe-flow computations.

As a more severe test for turbulent-flow calculations, the flow in the entrance region of a pipe was considered. The calculations were performed for a Reynolds number of 388,000 and an inlet velocity of 200 ft/sec using a 31x34 grid. The grid spacing near the wall was $\frac{\Delta r}{r_o} = 0.0005$, with r_o

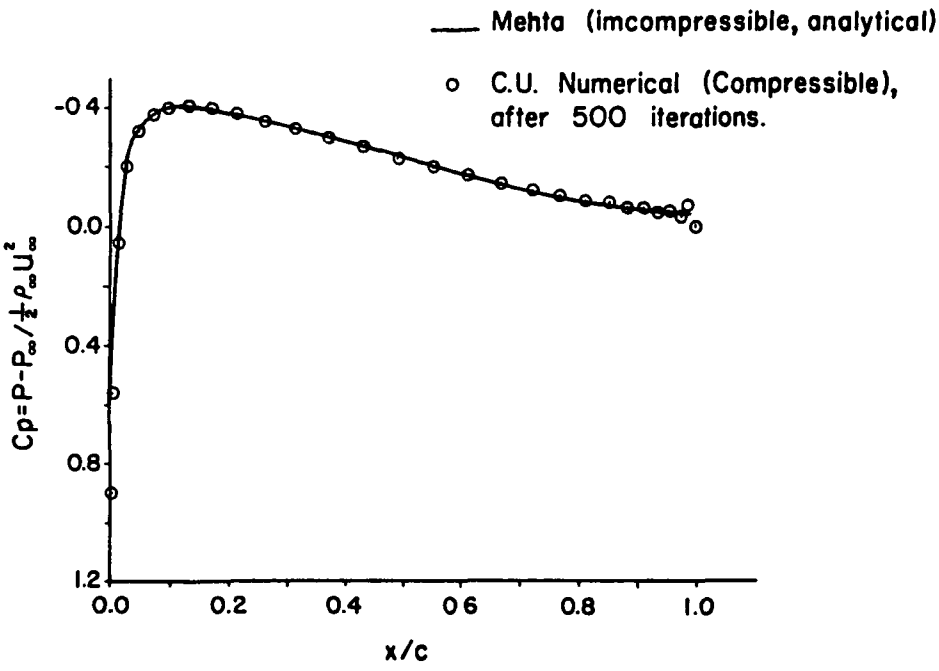

Figure 7. Pressure coefficient distribution, NACA 0012 airfoil, zero degree incidence, M=0.2 Re =10,000, laminar.

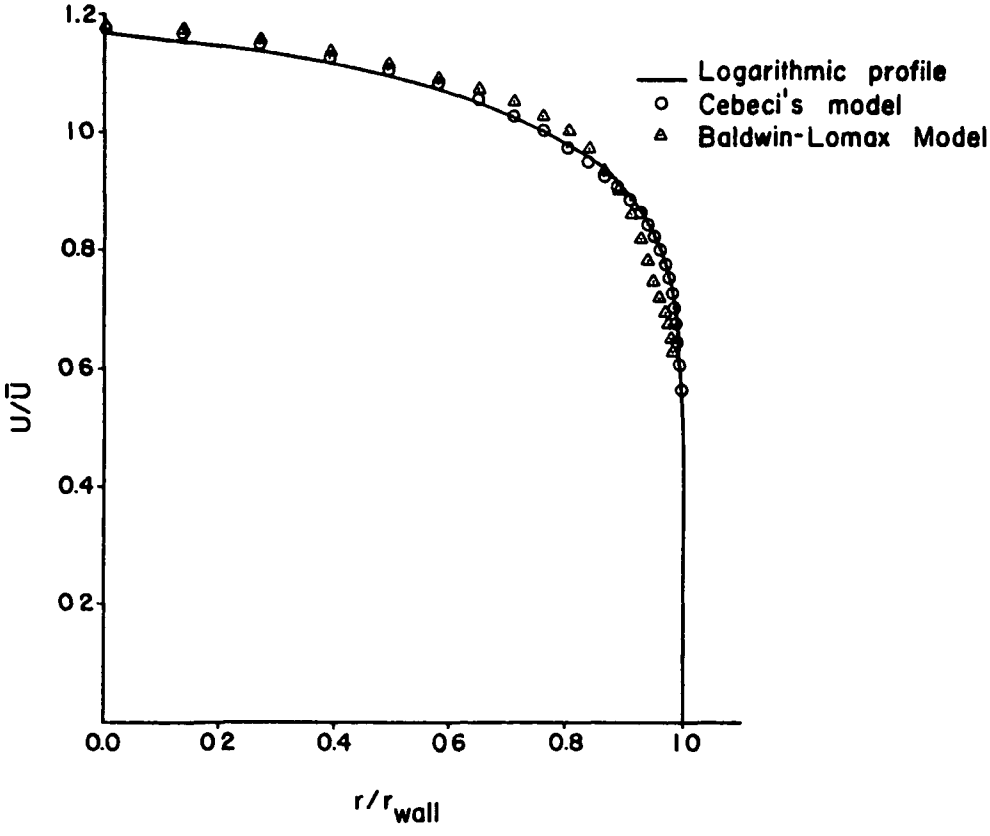

Figure 8. Fully developed flow in a circular pipe at Re_d=110,000.

being the pipe radius. This grid was stretched exponentially towards the centerline, in order to reduce computational time. In the x-direction, a uniform increment of one diameter was used. Due to the small grid near the wall, the time step for this problem had to be taken small enough to allow stable calculations from an impulsive start at uniform conditions. However, to accelerate the computations, the time step was increased by a factor of 20 after 100 iterations. The velocity results after 600 iterations are shown in Figure 9, along with the experimental data of Barbin and Jones (29), obtained at the same Reynolds number. The agreement is generally good, although the numerical solution (of Equation 3) indicates a slightly larger acceleration near the centerline. In Figure 10, the computed pressure distribution is compared to the experimental one. The experiment was performed on a pipe length of 45 diameters, while the calculations were performed on a pipe length of 30 diameters. For comparison, the reference pressure was arbitrarily taken as the exit pressure of the computations. In this case, the numerical solution deviates only slightly from the experimental data. This could partially be attributed to the imperfections of the turbulence model, and partly attributed to the difference in pipe length between computational and experimental cases.

3.1.2.2. Compressor cascade

The last case of the direct solution is the flow in a compressor cascade. The cascade blade geometry used in the calculations was the result of an analytical and experimental investigation by Schmidt et al. (7). Sorenson's code (9) was used to obtain the finite difference grid for the cascade. The grid is shown in Figure 11. It is a 79x34 grid of the C type, in which the vertical line on the extreme right represents the outflow boundary, and the vertical line at the extreme left, the inflow boundary. The outflow and

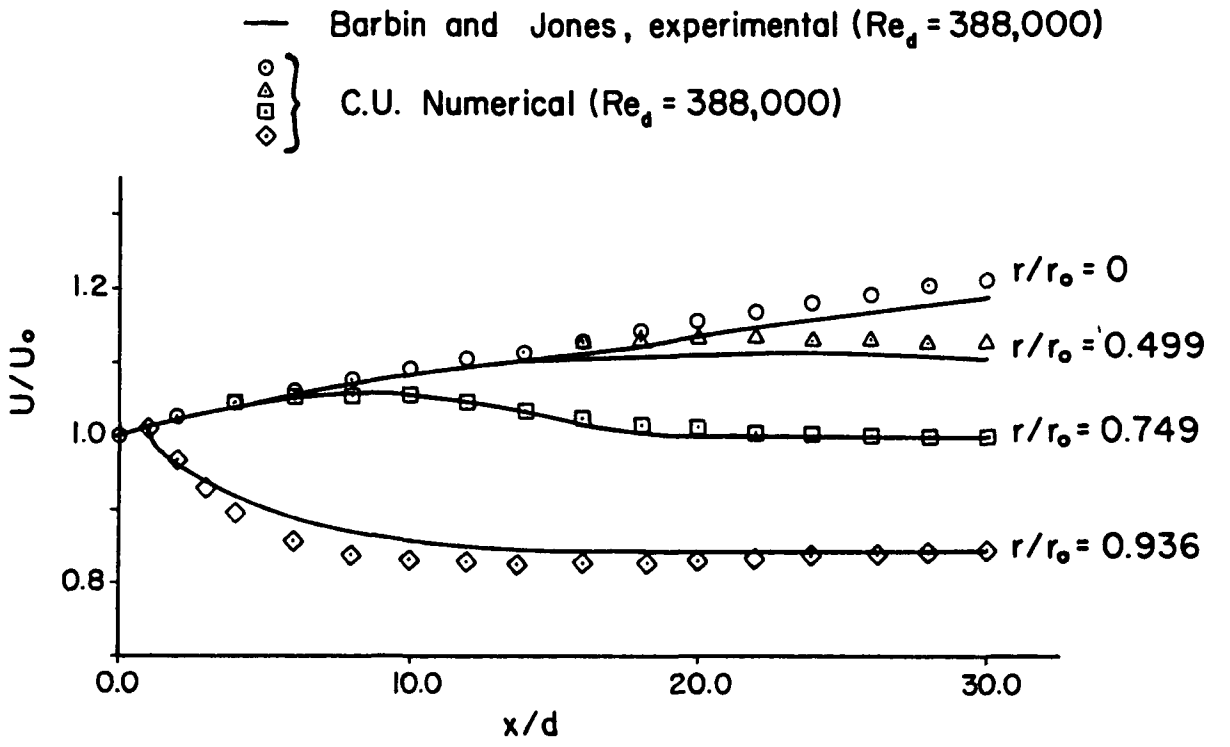

Figure 9. Entry of a circular pipe. Turbulent flow velocity distributions.

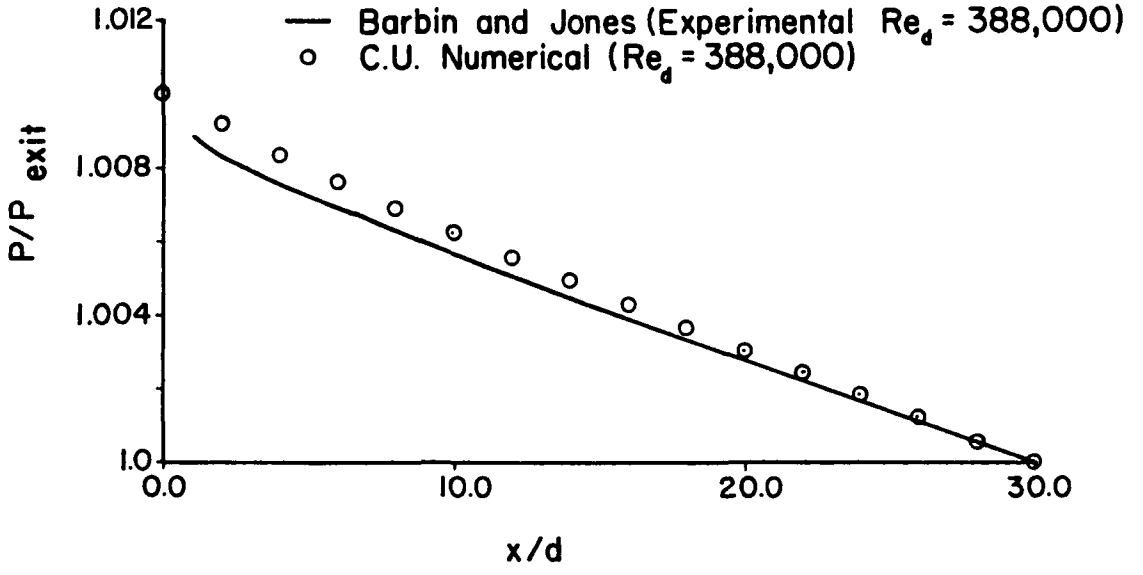

Figure 10. Entry region of a circular pipe. Turbulent flow pressure distributions.

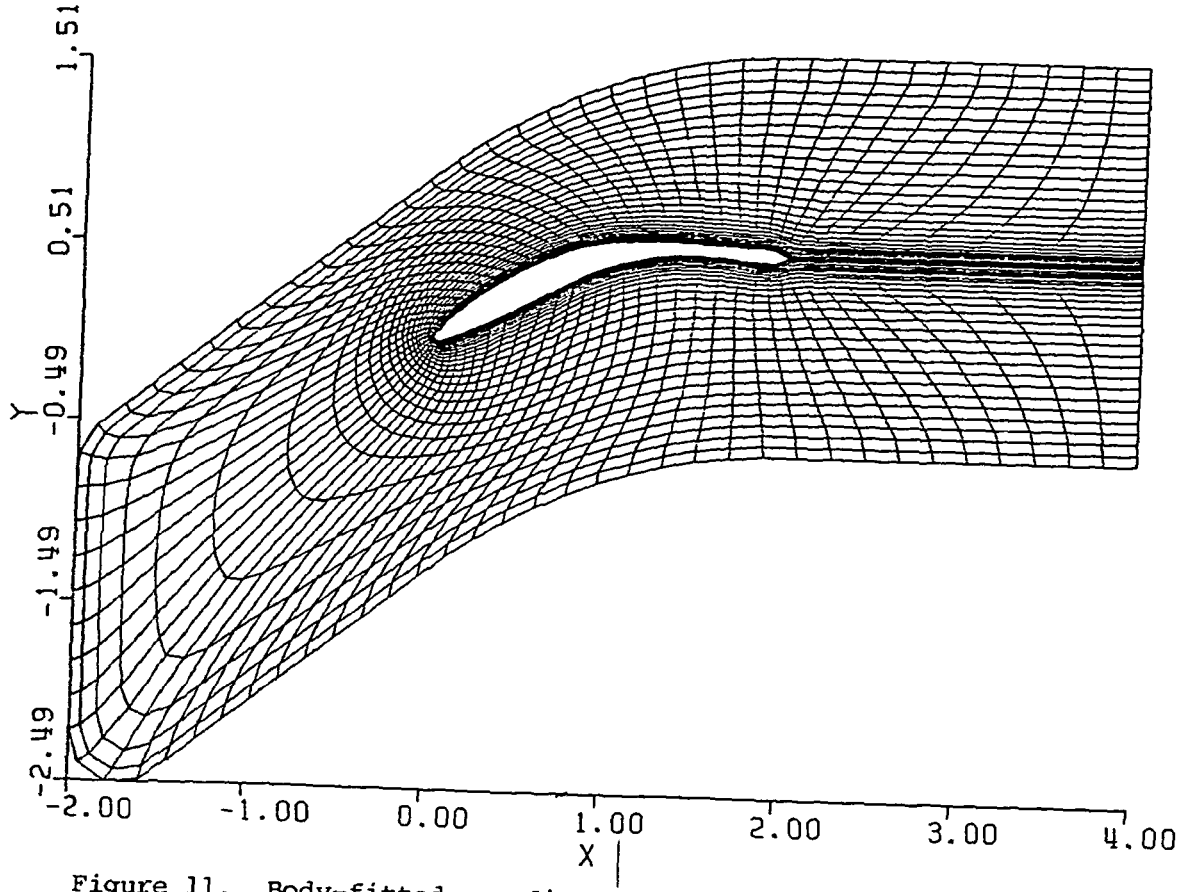

Figure 11. Body-fitted coordinates, compressor blade (ref. 7)

inflow boundaries are connected by two periodic boundaries maintained at a vertical distance equal to the cascade spacing from each other. It should be noted that the periodic boundaries are joined to the inlet boundary by circular arcs. For a clean separation between inlet and periodic boundaries, it seems desirable to keep the radius of those circular arcs as small as possible. However, it was found that trying to use a very small radius could make the grid generation calculations unstable.

The spacing maintained between the inner-boundary and the nearest ξ-line was approximately 0.00056. The blunt trailing edge of the airfoil was changed to a sharp trailing edge in order to allow a smooth stretching of the grid in the wake region (ξ-direction), without the need for additional points. This modification was not expected to significantly affect the solution away from the trailing edge.

The boundary conditions for the cascade problem were treated as described in the case of the isolated airfoil, except for the periodic boundaries. At the periodic boundaries, extrapolation from the interior (using $\frac{\partial}{\partial n} = 0$) was used for all variables. In order to maintain periodicity, the average values of the extrapolators from above and below were imposed at both boundaries.

The calculations were performed at a Reynolds number of 170,000, which is roughly a tenth of the Reynolds number of the experimental investigation of Reference 7. It was assumed that the solution at the lower Reynolds number would still represent the essential features of the solution at the higher Reynolds number. Attempting a high Reynolds number calculation would have required the use of a finer grid near the wall, and, therefore, a much larger number of grid points. This, combined with the smaller time steps

associated with finer grids, would have led to a much more expensive solution.

Convergence for the cascade problem was found to be quite slow, with large oscillations of the dependent variables in time. In particular, when ρ, u and v were specified at the inlet and the pressure extrapolated, large pressure fluctuations were observed at the inlet. Since those fluctuations did not seem to die out fast enough, this treatment of the inlet was abandoned in favor of the specification of the stagnation pressure and temperature and the flow angle (35.3°). Although oscillations were present in this inlet treatment as well, they were not as large, and they died out faster. However, in this case, the inlet Mach number cannot be specified but is determined from the specified inlet stagnation quantities and outflow static pressure. For given inlet stagnation quantities, the exact inlet Mach number will be obtained if the exact downstream pressure is specified. Since the exact values were not available at the required locations, the experimental inlet Mach number (0.75) could not be obtained without going through a trial-and-error procedure.

The results of the calculations shown in Figure 12 are for inlet Mach numbers of 0.734 and 0.77 measured at the inlet midpoint. Referring to Figure 12, comparison of the two computed Mach number curves suggests that for a given upstream stagnation conditions, a small change in downstream static pressure may result in a small change in inlet Mach number which in turn may have a significant effect on the solution. Therefore, one may expect that the non-uniform inlet Mach numberswill affect the solution. Since a uniform inlet Mach number only occurs when the inlet boundary is taken far enough from the airfoil, it is reasonable to expect that doing so might improve the results. Figure 13 shows a linear interpolated result for

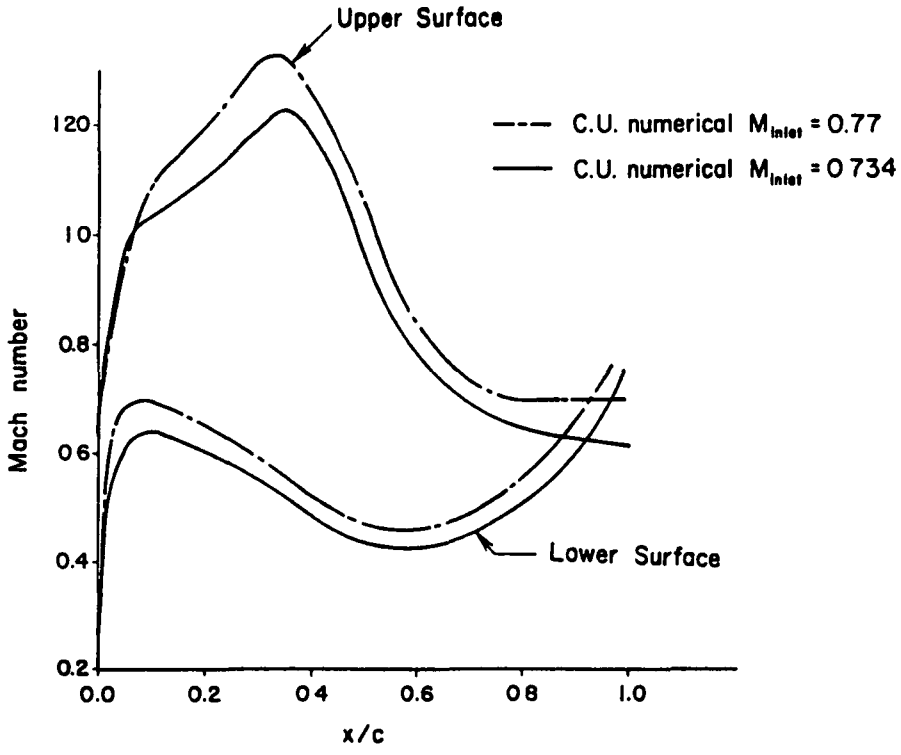

Figure 12. Surface Mach number distributions.

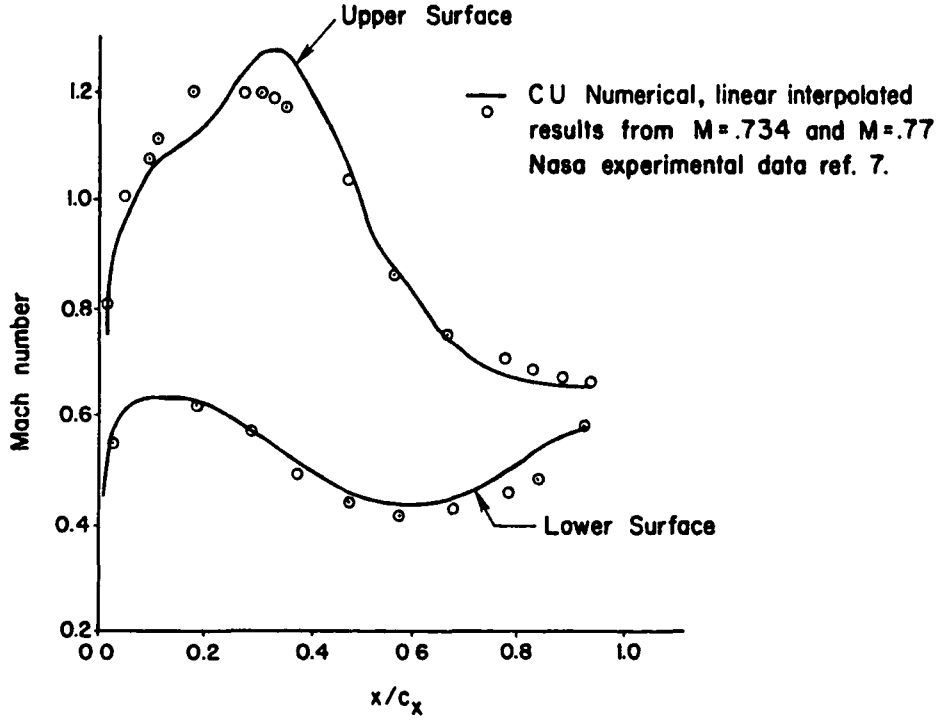

Figure 13. A comparison of surface Mach number distributions between interpolated numerical results and experimental data.

Figure 12 for inlet Mach number of 0.75. It is compared to the experimental data. The wall Mach numbers plotted in these figures were obtained from an isentropic relation between the inlet stagnation pressure and the wall static pressure. In general, Figure 13 shows that a good agreement exists between the computed and the experimental values with an inlet Mach number of 0.75. However, in all cases the computed peak Mach number seems too high.

Over the pressure side, which is the lower surface, the agreement between computed and experimental Mach number is very good for the first 60% of the chord. A maximum deviation of 10% occurs around 80% chord location. Over the suction side, the upper surface, deviations occur in the 15 to 40% chord region. The experimental peak seems to occur at 25% chord while the computed peak occurs at 30% chord. The maximum deviation, however, only amounts to 7%.

The flow compression takes place rapidly from 30% chord onward over the upper and lower surfaces. Some accleration occurs over the lower surface toward the trailing edge. This flow behavior is shown both computationally and experimentally. Because of the rapid compression, it is suspected that there might be a possibility of flow separation over the upper surface toward the trailing edge. The velocity field plot, shown as Figure 14, indicates that there is a small flow reversal and then a reattachment over that region.

Experience gained with the cascade calculations shows that care must be exercised in obtaining an adequate grid for the computations. The distribution of points along the airfoil must be such that the geometry is adequately represented.

Convergence for cascade direct computations may require 3000 to 5000 iterations from an impulsive start. Acceleration of the computations requires the use of large time steps. The non-dimensional time step $\Delta t'$

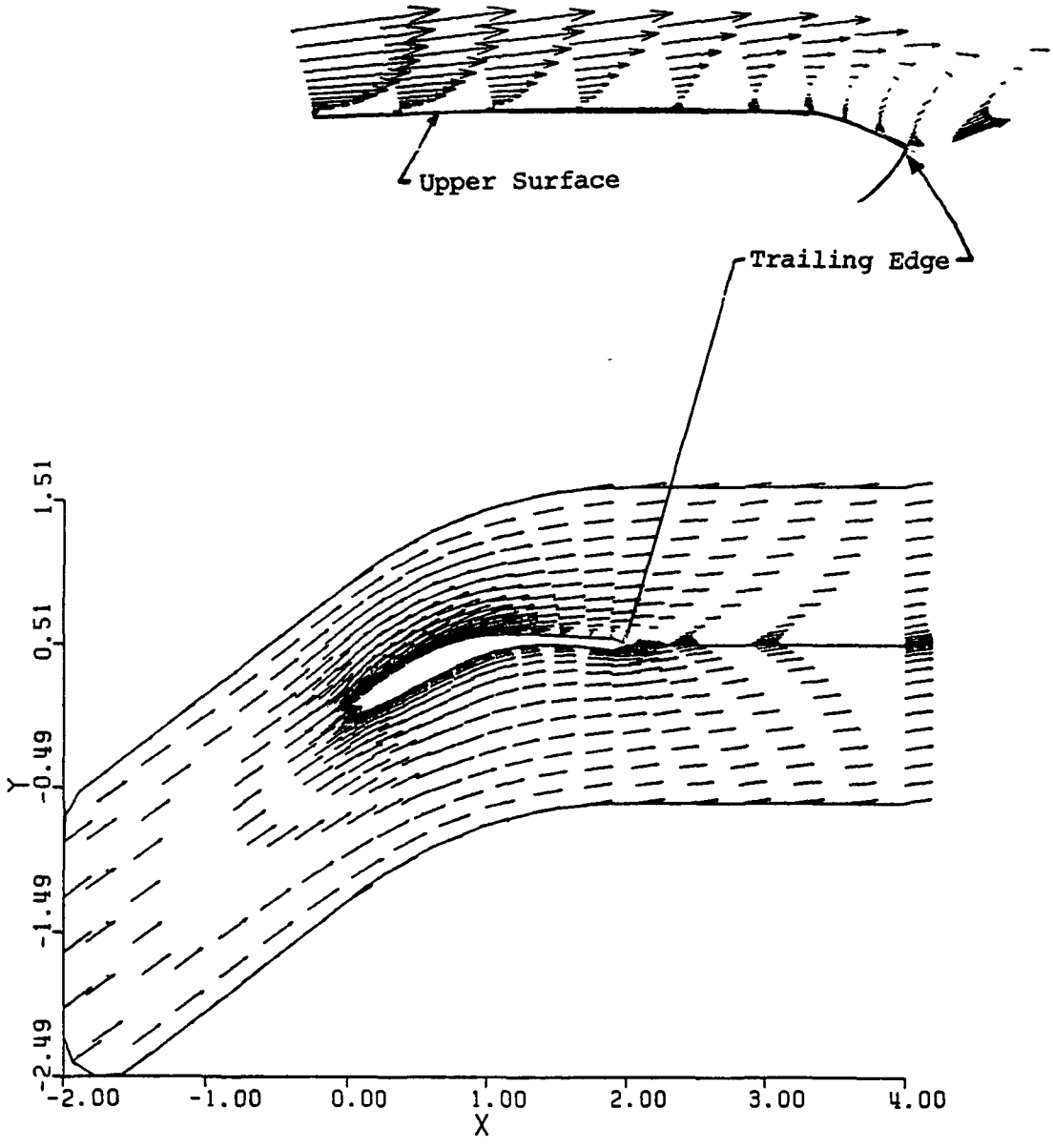

Figure 14. Velocity field between compression blades. Enlargement over the upper surface near the trailing edge showing flow reversal.

considered here varied from 0.001 to 0.02. However, large time steps require more smoothing for stability. Since excessive smoothing may lead to less accuracy, a careful balance must be kept in the choice of the time step and the smoothing coefficient (referred as ε_1, in section 2.5). Also, subsonic computations require less smoothing than computations involving transonic effects. It should be noted that upwind differencing has not been incorporated in the code. Therefore, the code is not quite ready for transonic computations. This may explain some of the discrepancies observed in Figure 13 where the wall Mach number exceeds 1. On the IBM 3081 and for a 79x34 grid, roughly 4.2 seconds of CPU time are required for each iteration.

3.2 Inverse Solution Examples

The illustrations presented for the direct solution were designed to show that good results can be obtained for a variety of cases. For the design problem, it is assumed that the direct solver is good, and the success of the inverse methods presented earlier is judged by their ability to produce a wall geometry that yields a pressure distribution close to a target distribution.

3.2.1 Secant Method

An axisymmetric nozzle with a wavy wall geometry as shown in Figure 15 was selected for sample calculations. The corresponding pressure distribution, as calculated by the direct solver, is shown in Figure 16. This pressure distribution, along with the two initial geometry guesses shown in Figure 15, were input to the design calculations. Figures 15 and 16 show the convergence histories for the wall geometry and the wall pressure, respectively. It is seen from those figures that a good design can be obtained with a small number of wall corrections. In this case, the calculations were started with uniform flow conditions prescribed on the

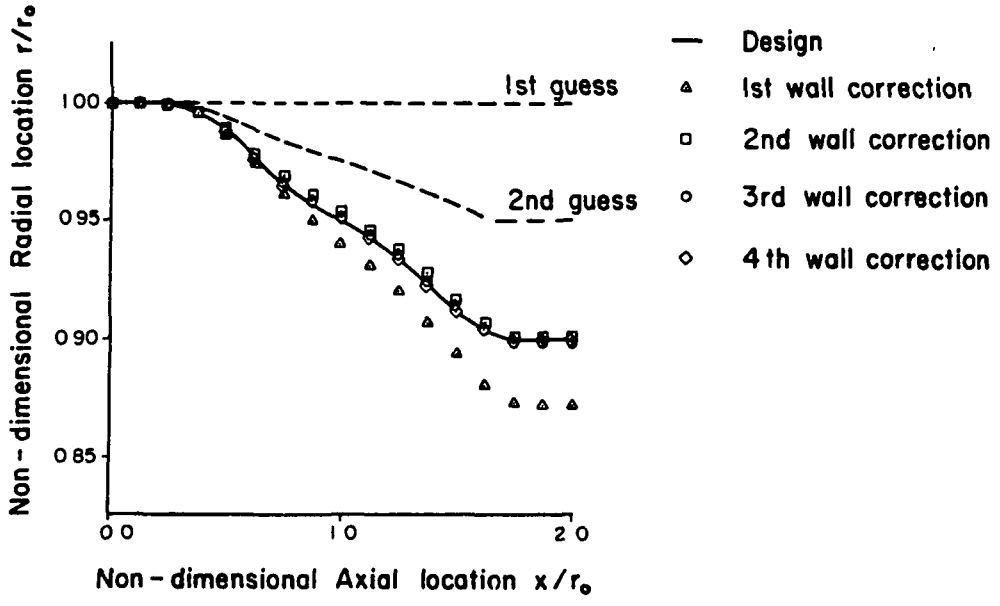

Figure 15. Wall geometry at various interation levels. Secant method applied to a nozzle at Re_d =24.

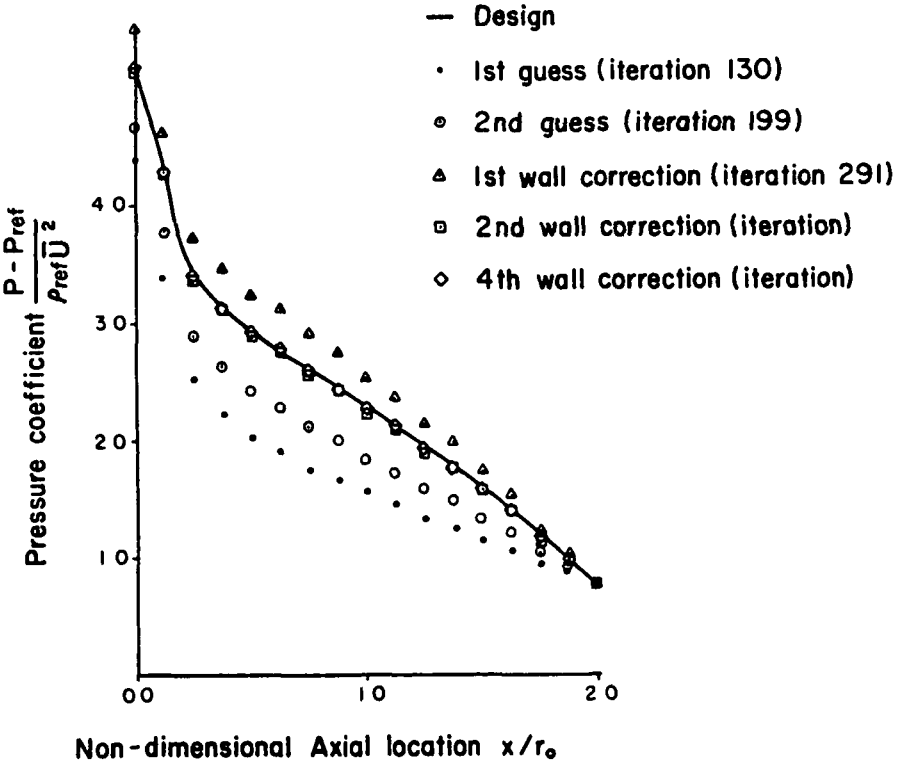

Figure 16. Wall pressure at various iteration levels. Secant method applied to a nozzle at re_d=24.

first guess-geometry. The value of σ_p was kept constant throughout the calculations, but was selected small enough to allow accurate results. The 449 direct solver iterations required for the problem are not excessive, given that the direct solution for a single geometry would require about 200 iterations.

3.2.2 Virtual Wall Velocity Method

3.2.2.1. Flow nozzle

The nature of the virtual wall velocity method restricts its use to problems in which the region to be corrected lies between two fixed points. For example, its use for a nozzle design problem may assume that the locations of the inlet and exit radii are fixed, and the interior part is to be redesigned.

This method was applied to a nozzle design problem as shown in Figure 17. In that figure, the target geometry is shown as a solid line, and corresponds to the pressure distribution shown as a solid line in Figure 18. The pressure distribution was input to the design calculations as a target pressure, and the geometry shown as a broken line in Figure 17 was used as an initial guess. The best geometry, represented by the circles, was obtained after 15 wall corrections and 670 iterations of the direct solver, which shows that this method is somewhat slower than the previous method. The corresponding pressure distribution, shown by the circles in Figure 18, is quite close to the target pressure.

In order to check if results could be obtained with an initial geometry taken farther from the correct geometry than in the above case, the same problem was restarted with an initial geometry as shown in Figure 19. The best computed geometry, obtained after 22 wall corrections (700 direct solver iterations), is also shown in Figure 19. Here as before, the corresponding

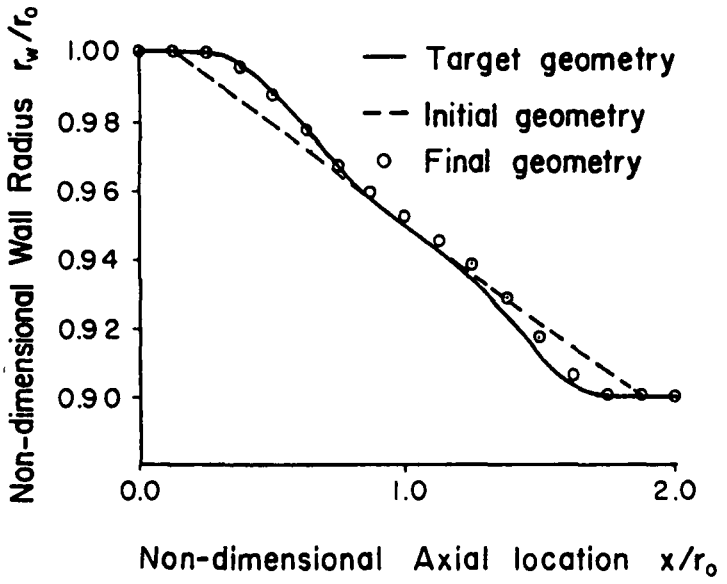

Figure 17. Wall geometry at various iteration levels. Virtual velocity inverse method applied to a nozzle at Re_d=24.

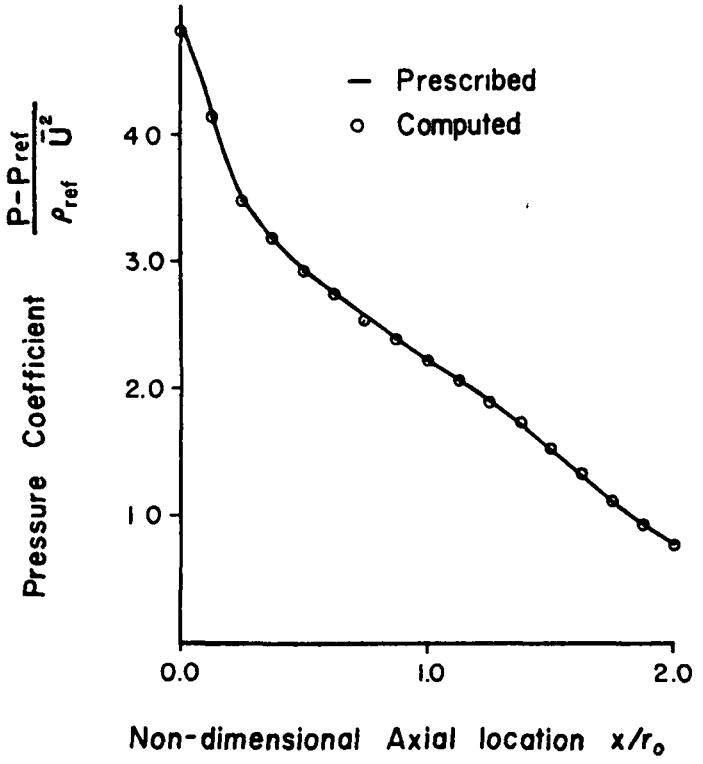

Figure 18. Wall pressure distribution prescribed versus computed. Virtual velocity inverse method applied to a nozzle at Re_d=24.

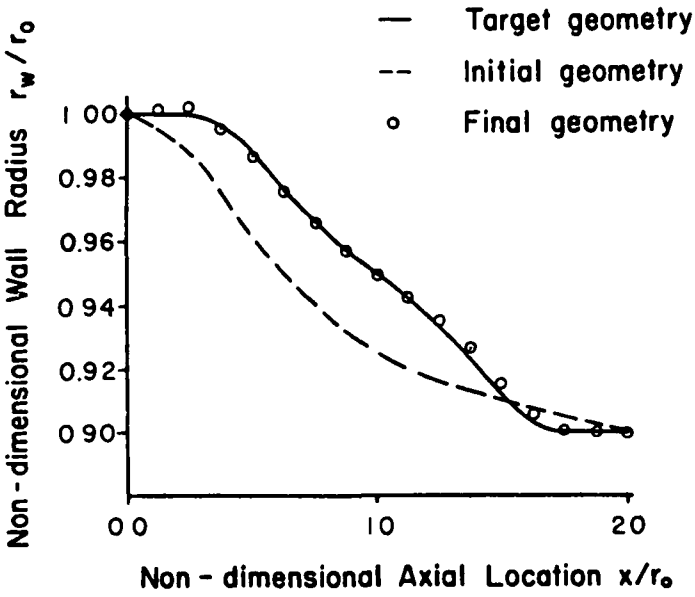

Figure 19. Wall geometry at various iteration levels. Virtual velocity inverse method applied to a nozzle at Re_d=24.

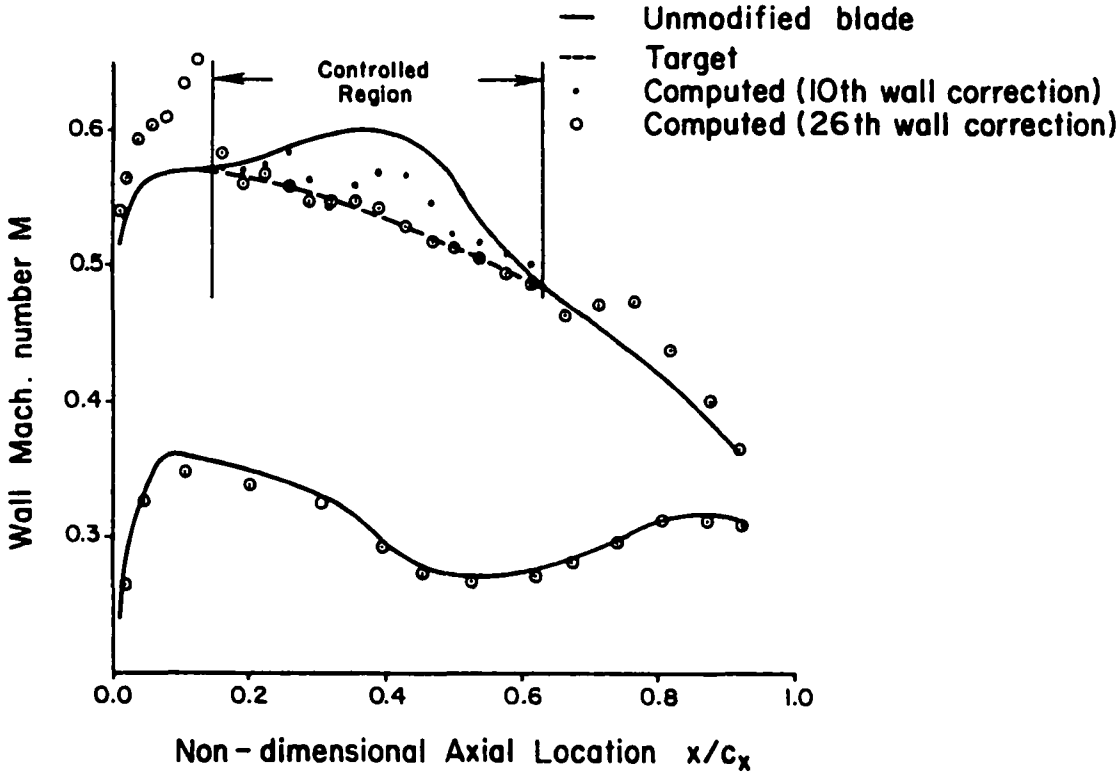

Figure 20. Wall mach number distribution at various iteration levels. Virtual velocity inverse method applied to a portion of a compressor cascade. Inlet mach number 0.44.

pressure was quite close to the target pressure. In the above cases, $\lambda = 0.2$ was used and the sign of the R.H.S. of equation 17 was taken as positive if p^d was greater than p and negative otherwise. More illustration may be found in reference 30.

3.2.2.2. Redesign of Compressor Cascade Blade

Since the relationship between pressure and wall geometry may become quite complicated in a cascade problem, the selection of two initial guess-geometries may not be as easy in this case as it is in nozzle or diffuser flows. For that reason, the virtual wall velocity method was selected for use in cascade computations. In order to test the method, the compressor cascade previously described for direct computations was again considered, with the inlet Mach number reduced to 0.44 so that transonic behavior could be avoided. The wall Mach number from a direct computation on the unmodified cascade is shown in Figure 20. For the design calculations, it was decided that the upper surface Mach number "bump", as seen in Figure 20, be removed. The wall correction method was applied only in that portion of the blade, and the rest of the geometry was kept the same as for the unmodified blade. Such a modification only serves the purpose of illustrating the inverse design, and it is understood that in most cases, one may need to increase the area inside the Mach number curve rather than decrease it.

For the cascade computations, λ was not kept constant, but was calculated as

$$\lambda = \lambda' \left(\frac{p^d - p}{\rho}\right)^{1/2}$$

where λ' is specified. The desired effect of this modification was to emphasize the difference between small and large values of $|\Delta r|$ calculated from Equation (17). Particularly, geometry corrections near the junctions

between the specified geometry region and the specified pressure region were to be made smaller, while corrections inside the specified pressure area (where $| P^d - P |$ is larger) were to be made comparatively larger.

The design calculations were initiated using the unmodified cascade and its converged solution. After each wall correction, the new geometry was manually input to Sorenson's Grape code to obtain a new grid. It should be noted that making the process fully automatic requires coupling of the grid program with the Navier-Stokes code). After the 6th wall correction, λ' was increased from 0.5 to 0.9 to accelerate the process. The final Mach number distribution shown in Figure 20 was obtained after 26 wall corrections (4,800 iterations). It is quite close to the target distribution, and could have been made even closer by allowing for more wall corrections. The corresponding geometry modification is shown in Figure 21.

Examination of the wall Mach number history after each wall correction reveals that the wall Mach number in the region being modified behaves in a wave-like manner. A wavy wall Mach number distribution such as the one shown in Figure 20 (10th wall correction) is typical. The waves are generated at the right side of the region being modified and move to the left, where they tend to vanish. The process will be stable if the amplitude of each new wave is smaller than the previous one.

The speed of the calculations is controlled by both $\Delta t'$ and λ'. Since $\Delta t'$ is usually limited by stability requirements for the direct solver, acceleration of the inverse process is obtained by varying λ'. At this point, the upper limit for λ' has not been established as yet.

At the junctions between the region of specified geometry and the region of specified pressure, little control can be exercised over the pressure distribution, as shown by the Mach number spike on the left side of the

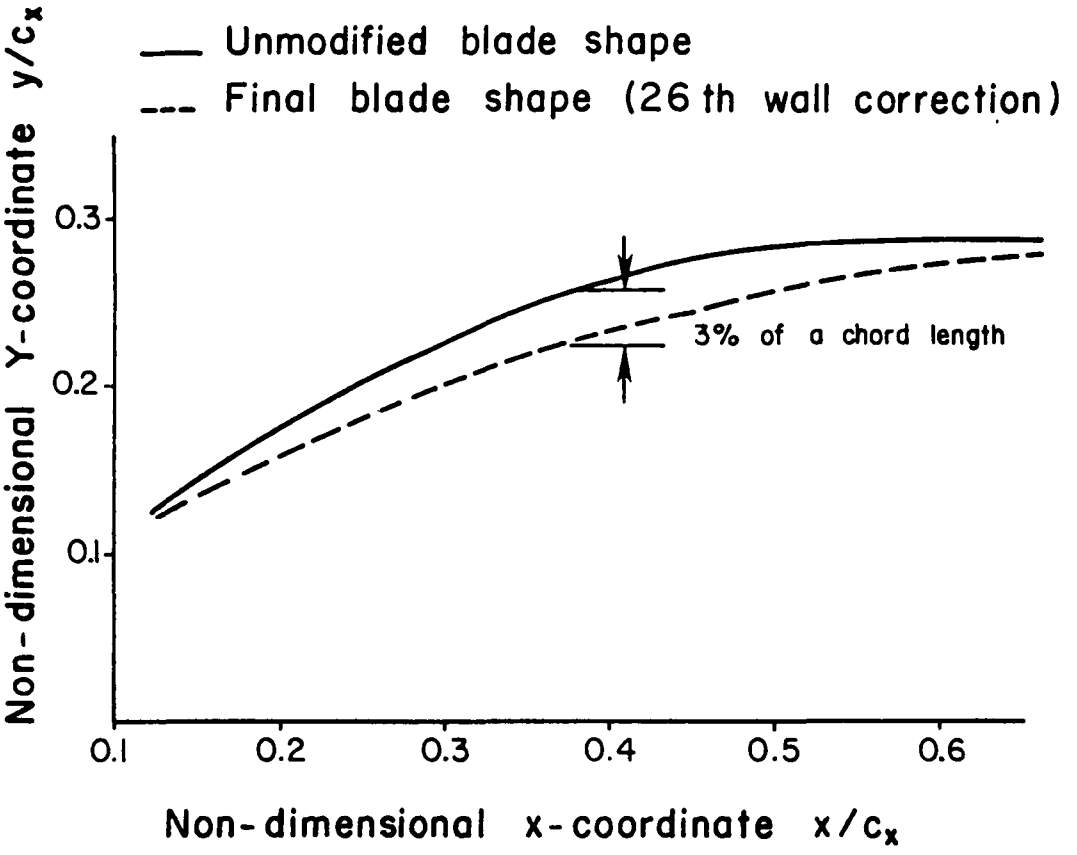

Figure 21. A portion of blade shapes before and after modification.

corrected region. Similar behavior has been reported in Reference 31. Removal of such a spike can be done by independent smoothing of the geometry or by extending the region of specified pressure.

In the cascade computations, the sign of the right hand side of Equation (17) was taken as positive for $P^d < P$ and negative for $P^d > P$. The method works well for subsonic cases. However, for transonic calculations where small changes in geometry may lead to substantial changes in flow behavior, particularly when shocks are present, a more elaborate way of determining the sign of the wall correction may be required.

4. Conclusions

The following objectives of this research were achieved:

1. An implicit factored algorithm was applied to the two-dimensional (axisymmetric and planar) thin layer Navier-Stokes equations. Good results were obtained for a variety of cases.

2. Two methods for using the direct solver as an inverse design tool have been examined. The method of virtual velocity was used for compressor re-design calculations. In the re-design illustration, 26 wall corrections or 4800 time-steps were required to yield the final geometry. The rate of convergence is considered quite acceptable.

5. Recommendations for Future Work

It is believed that if one gains more experience in using the direct solver one may obtain more accurate results with less computation time. Also, improvements can be made for more efficiency and better accuracy. For example, adaptation of the algorithm to vectorized computers may lead to substantial savings in computer time. Introduction of upwind differencing would lead to a better handling of shock waves in transonic flows. For flows with supersonic inflow or outflow boundaries, conditions compatible with the supersonic nature of the flow will have to be imposed. Also, higher level turbulence models can be used, and extensions to the three-dimensional case are desirable.

6. References

1. Stanitz, J. D., "Design of Two-Dimensional Channel with Prescribed Velocity Distributions Along the Channel Walls," NACA Report 1115, 1953.

2. Yang, Tah-teh, Hudson, William G., and Nelson, Carl D., "Design and Experimental Performance of Short Curved Wall Diffusers with Axial Symmetry Utilizing Slot Suction," NASA CR-2209, March 1973.

3. Yang, Tah-teh and Nelson, Carl D., "Griffith Diffusers," Journal of Fluids Engineering, Vol. 101, No. 1, December 1979.

4. Yang, Tah-teh, Ntone, Francois, Jiang, Tong, and Pitts, D. R., "An Investigation of High Performance, Short Thrust Augmenting Ejectors," Journal of Fluids Engineering, Vol. 107, No. 1, March 1985.

5. Baldwin, B. S., and Lomax, H., "Thin Layer Approximation and Algebraic Model for Separated Turbulent Flows," AIAA Paper 78-257 presented at AIAA 16th Aerospace Sciences Meeting at Huntsville, Alabama, January 1978.

6. Cebeci, T., Smith, A. M. O., and Mosinskis, G., "Calculation of Compressible Adiabatic Turbulent Boundary Layers," AIAA Journal, Vol. 8, No. 11, November 1974.

7. Schmidt, James F., Gelder, Thomas F. and Donovan, Leo F., "Redesign and Cascade Tests of a Supercritical Controlled Diffusion Stator Blade-Section," NASA TM 83635, 1984.

8. Thompson, J. F., Thames, F. C., and Martin, C. W., "Automatic Numerical Generation of Body-Fitted Curvilinear Coordinate System for Field Containing Any Number of Arbitrary Two-Dimensional Bodies," Journal of Computational Physics, Vol. 15, No. 3, July 1974.

9. Sorenson, R. L., "A Computer Program to Generate Two-Dimensional Grids About Airfoil and Other Shapes by the Use of Poisson's Equation," NASA TM-81198, 1980.

10. Beam, R. M. and Warming, R. F., "An Implicit Finite-Difference Algorithm for Hyperbolic Systems in Conservation Law Form," Journal of Computational Physics, Vol. 22, No. 1, Sept. 1976.

11. Steger, J. L., "Implicit Finite-Difference Simulation of Flow About Arbitrary Two-Dimensional Geometries," AIAA Journal, Vol. 16, No. 7, July 1978.

12. Forsythe, G. E., Malcolm, M. A. and Moler, C. B., Computer Methods for Mathematical Computation, Prentice-Hall Inc., 1977.

13. Thompkins, W. T., Jr. and Tong, S. S., "Inverse or Design Calculations for Nonpotential Flow in Turbomachinery Blade Passages," Journal of Engineering for Power, Vol. 104, No. 2, April 1982.

14. Ntone, Francois, "Direct and Inverse Calculations with Viscous Compressible Flow Theory," Ph.D. Dissertation, Clemson University, 1985.

15. Peyret, R., and Viviand,H., "Computation of Viscous Compressible Flow Based on the Navier-Stokes Equations," AGARD-AG-212, 1975.

16. Farre, A., "Equations des Gaz Turbulents Compressibles," Journal de Mecanique, Vol. 4, No. 3, Sept. 1965.

17. Rubesin, M. W. and Rose, W. C., "The Turbulent Mean-Flow, Reynolds Stress, and Heat Flux Equations in Mass-Averaged Dependent Variables," NASA TM X-62248, March 1973.

18. Rubesin, M. W., "Numerical Turbulence Modeling," AGARD Lecture Series No. 86, April 1977.

19. Degani, D. and Steger, J. L., "Comparison Between Navier-Stokes and Thin-Layer Computations for Separated Supersonic Flow," AIAA Journal, Vol. 21, No. 11, November 1983.

20. Moretti, G., "Importance of Boundary Conditions in the Numerical Treatment of Hyperbolic Equations," The Physics of Fluids Supplement II, 1969.

21. "Numerical Boundary Condition Procedures," NASA Conference Publication 2201, A symposium held at AMES Research Center, Moffett Field, Oct. 19-20, 1981.

22. Desideri, J. A., Steger, J. L., and Taunehill, J. C., "On Improving the Iterative Convergence Properties of an Implicit Approximate-Factorization Finite Difference Algorithm," NASA TM-78495, June 1978.

23. Beam, R. M. and Warming, R. F., "An Implicit Factored Scheme for the Compressible Navier-Stokes Equations," AIAA Journal, Vol. 16, No. 4, April 1978.

24. Schlichting, H., Boundary Layer Theory, 6th Edition, McGraw-Hill, 1968, pp. 83-84.

25. Friedman, M., Gillis, J. and Lison, N., "Laminar Flow in a Pipe at Low and Moderate Reynolds Numbers," Applied Scientific Research, Vol. 19, No. 6, Nov. 1968.

26. Tietjens, O. G., Applied Hydro- and Aeromechanics, First Edition, McGraw-Hill, New York, 1934.

27. Campbell, W. D. and Slattery, J. C., "Flow in the Entrance of a Tube," Journal of Basic Engineering, Vol. 85, No. 1, March 1963.

28. Sparrow, E. M., Lin, S. H. and Lundgren, T. S., "Flow Development in the Hydrodynamic Entrance Region of Tubes and Ducts," The Physics of Fluids, Vol. 7, No. 3, March 1964.

29. Barbin, A. R., and Jones, J. B., "Turbulent Flow in the Inlet of a Smooth Pipe," Journal of Basic Engineering, Vol. 85, No. 1, March 1963.

30. Proceedings of International Conference on Inverse Design Concepts in Engineering Sciences, Oct. 17-18, 1984, pp. 387-396.

31. Greitzer, E. M., Thompkins, W. T., Sr., McCure, J. E., Epstein, A. H., Tan, C. S., and Hawthorne, W. R., "Current Problems in Turbomachinery Fluid Dynamics," AFOSR-TR-82-0027, November 1981.

APPENDIX A

Body-Fitted Coordinate System

In order to have boundary conditions satisfied exactly over an arbitrary shaped body, the Navier-Stokes equations are written in a transformed coordinate system such that the boundaries of the flow field correspond to grid lines of the finite difference network. In this Appendix, a method of obtaining such a transformation is explained.

Following Thompson et al. (8), one may define a coordinate transformation from a physical plane (x, r) to a computational plane (ξ, η) so that the computational and physical coordinates are related by the Poisson equation:

$$\xi_{xx} + \xi_{rr} = f(\xi,\eta)$$

$$\eta_{xx} + \eta_{rr} = g(\xi,\eta) \ . \qquad \text{(A1)}$$

In the above, f and g are forcing functions to be specified. In practical problems, it is often desired to define a computational grid work in a rectangular, uniform, transformed plane. Equations (A1) are therefore rewritten so that ξ and η become the independent variables:

$$\alpha\, x_{\xi\xi} - 2\,\beta x_{\xi\eta} + \gamma\, x_{\eta\eta} + \frac{1}{J^2}(f x_{\xi} + g\, x_{\eta}) = 0$$

$$\alpha\, r_{\xi\xi} - 2\,\beta r_{\xi\eta} + \gamma\, r_{\eta\eta} + \frac{1}{J^2}(f r_{\xi} + g\, r_{\eta}) = 0 \qquad \text{(A2)}$$

where

$$\alpha = x_{\eta}^2 + r_{\eta}^2 \ , \quad \gamma = x_{\xi}^2 + r_{\xi}^2$$

$$\beta = x_{\xi}x_{\eta} + r_{\xi}r_{\eta} \ , \quad J = \frac{1}{x_{\xi}\, r_{\eta} - x_{\eta}\, r_{\xi}} = \xi_x\eta_r - \xi_r\eta_x$$

and

$$\xi_x = J\, r_\eta \quad , \quad \xi_r = -Jx_\eta \, ,$$

$$\eta_x = -J\, r_\xi \quad , \quad \eta_r = Jx_\xi \tag{A3}$$

Equations (A2) are a set of elliptic partial differential equations. If a set of values for x and r are specified at the boundaries of the region of interest, these equations can be solved numerically by using, for example, an SOR (successive over relaxation) or an LSOR (line successive over relaxation) technique.

As mentioned earlier, f and g must be specified. If one selects f = g = 0, equations (A1) reduce to a set of Laplace equations, and the solution of Equations (A2) yields a highly uniform distribution of grid lines as viewed in the physical plane. If a non-uniform grid is desired, for example when one needs a fine grid near a wall, which gets coarser as one moves away from the wall, then one must find a method of specifying f and g. Steger and Sorenson (9, 11) using the exponential form of f and g suggested by Thompson, derived a method of specifying the forcing functions so that orthogonality and a specified spacing can be maintained near the boundaries. According to this method, f and g have the following form:

$$f(\xi,\eta) = f_1(\xi)\, e^{-a\eta} + f_2(\xi)\, e^{-c(\eta_{max} - \eta)}$$

$$g(\xi,\eta) = g_1(\xi)\, e^{-b\eta} + g_2(\xi)\, e^{-d(\eta_{max} - \eta)} \, , \tag{A4}$$

where f_1, f_1, g_1, g_1 are positive constants which must be calculated so that four geometric constraints are satisfied, and a, b, c and d are positive constants to be specified.

The third and fourth constraints are the same as the first two, except that they are applied to the boundary $j=j_{max}$ (outer boundary). They lead to two equations similar to (10) for $x_\eta|_{j=j_{max}}$ and $r_\eta|_{j=j_{max}}$.

Now considering the boundary j=1 ($\eta=0$), it is clear, since η_{max} is large, that Equations (A4) reduce to

$$f(\xi,0) = f_1(\xi)$$

$$g(\xi,0) = g_1(\xi) \tag{A11}$$

Assuming that Equations (A2) apply at the boundary j=1, one may obtain expressions for $f_1(\xi)$ and $f_2(\xi)$ by combining (A2) and (A11):

$$f_1(\xi) = [J(r_\eta h_1 - x_\eta h_2)]_{j=1}$$

$$g_1(\xi) = [J(-r_\xi h_1 + x_\xi h_2)]_{j=1} \quad , \tag{A12}$$

where

$$h_1 = [-J^2(\alpha\, x_{\xi\xi} - 2\beta\, x_{\xi\eta} + \gamma x_{\eta\eta})]_{j=1}$$

$$h_2 = [-J^2(\alpha\, r_{\xi\xi} - 2\beta\, r_{\xi\eta} + \gamma r_{\eta\eta})]_{j=1} \; .$$

In the above equations, x_η and r_η are obtained from Equations (A10). A similar procedure applied to the outer boundary allows one to obtain expressions for $f_2(\xi)$ and $g_2(\xi)$. Then for specified values of a, b, c, d, $f(\xi,\eta)$ and $g(\xi,\eta)$ are known functions which can be used in the solution of Equations (A2). For details on the solution procedure, the reader is referred to Reference 9.

In this research, a computer code was written to solve Equation (A2), both with f=g=0 and with f and g specified as explained above. The code was

tested on simple cases. However, for complicated viscous grids such as for airfoil cascade calculation Sorenson's Grape code is used (Ref. 9).

APPENDIX B

Matrices used in the Numerical Algorithm

In this appendix, the matrices used in the algorithm for the thin layer Navier-Stokes equations are presented. Equations (12) and (13) of the text were derived for the numerical solution of Equation (1) of the text. All the matrices involved are listed as follows:

$$A = -\begin{bmatrix} 0 & -1 & 0 & 0 \\ \frac{3-\gamma}{2}u^2 + \frac{1-\gamma}{2}v^2 & (\gamma-3)u & (\gamma-1)v & 1-\gamma \\ uv & -v & -u & 0 \\ \frac{\gamma eu}{\rho} + (1-\gamma)\,u\,(u^2+v^2) & -\frac{\gamma e}{\rho} + \frac{\gamma-1}{2}(3u^2+v^2) & (\gamma-1)uv & -\gamma u \end{bmatrix}$$

$$B = -\begin{bmatrix} 0 & 0 & -1 & 0 \\ uv & -v & -u & 0 \\ \frac{3-\gamma}{2}v^2 + \frac{1-\gamma}{2}u^2 & (\gamma-1)u & (\gamma-3)v & 1-\gamma \\ \frac{\gamma eu}{\rho} + (1-\gamma)\,v\,(u^2+v^2) & (\gamma-1)\,uv & -\frac{\gamma e}{\rho} + \frac{\gamma-1}{2}(3v^2+u^2) & -\gamma v \end{bmatrix}$$

From the definition of $\tilde{A}$ and $\tilde{B}$ we can show that

$$\tilde{A} = \begin{bmatrix} 0 & \xi_x & \xi_r & 0 \\ -\xi_x\left(\frac{3-\gamma}{2}u^2 + \frac{1-\gamma}{2}v^2\right) & -\xi_x(\gamma-3)u & -\xi_x(\gamma-1)\,v & -\xi_x(1-\gamma) \\ -\xi_r uv & +\xi_r v & +\xi_r u & \\ -\xi_x uv - \xi_r\left(\frac{3-\gamma}{2}u^2 + \frac{1-\gamma}{2}v^2\right) & \xi_x v - \xi_r(\gamma-1)u & \xi_x u - \xi_r(\gamma-3)v & -\xi_r(1-\gamma) \\ -\xi_x\left[\frac{\gamma eu}{\rho} + (1-\gamma)u(u^2+v^2)\right] & -\xi_x\left[\frac{-\gamma e}{\rho} + \frac{\gamma-1}{2}(3u^2+v^2)\right] & -\xi_x(\gamma-1)uv & \gamma(\xi_x u+\xi_r v) \\ -\xi_r\left[\frac{\gamma ev}{\rho} + (1-\gamma)v(u^2+v^2)\right] & -\xi_r(\gamma-1)uv & -\xi_r\left[\frac{-\gamma e}{\rho} + \frac{\gamma-1}{2}(3v^2+u^2)\right] & \end{bmatrix}$$

$\tilde{B}$ is obtained from $\tilde{A}$ by replacing ξ_x by η_x and ξ_r by η_r.

Let $\alpha_1 = \mu\left(\frac{4}{3}\eta_x^2 + \eta_r^2\right)$ $\qquad$ $\alpha_2 = \frac{1}{3}\mu\eta_x\eta_r$

$\alpha_3 = \mu\left(\eta_x^2 + \frac{4}{3}\eta_r^2\right)$ $\qquad$ $\alpha_4 = \gamma\frac{\mu}{Pr}\left(\eta_x^2 + \eta_r^2\right)$

$$a_{1_{i,j}} = \left(\frac{\alpha_1 r}{J}\right)_{i,j+1} + 2\left(\frac{\alpha_1 r}{J}\right)_{i,j} + \left(\frac{\alpha_1 r}{J}\right)_{i,j-1}$$

$$a_{1_{i,j+1}} = \left(\frac{\alpha_1 r}{J}\right)_{i,j+1} + \left(\frac{\alpha_1 r}{J}\right)_{i,j}$$

$$a_{1_{i,j-1}} = \left(\frac{\alpha_1 r}{J}\right)_{i,j} + \left(\frac{\alpha_1 r}{J}\right)_{i,j-1}$$

$$a_{2_{i,j}} = \left(\frac{\alpha_2 r}{J}\right)_{i,j+1} + 2\left(\frac{\alpha_2 r}{J}\right)_{i,j} + \left(\frac{\alpha_2 r}{J}\right)_{i,j-1}$$

$$a_{2_{i,j+1}} = \left(\frac{\alpha_2 r}{J}\right)_{i,j+1} + \left(\frac{\alpha_2 r}{J}\right)_{i,j}$$

$$a_{2_{i,j-1}} = \left(\frac{\alpha_2 r}{J}\right)_{i,j} + \left(\frac{\alpha_2 r}{J}\right)_{i,j-1}$$

$a_{3_{i,j}}$ is obtained by replacing the subscript 1 of $a_{1_{i,j}}$ to 3

$a_{3_{i,j+1}}$ is obtained by replacing the subscript 1 of $a_{1_{i,j+1}}$ to 3

$a_{3_{i,j-1}}$ is obtained by replacing the subscript 1 of $a_{1_{i,j-1}}$ to 3

Similarly $a_{4_{i,j}}$, $a_{4_{i,j+1}}$ and $a_{4_{i,j-1}}$ may be obtained.

then

$$\overline{M} = \left[\begin{array}{c|c|c|c} 0 & 0 & 0 & 0 \\ \hline -\alpha_1 \frac{\partial}{\partial\eta}\left(\frac{Ju}{r\rho}\right) - \alpha_2 \frac{\partial}{\partial\eta}\left(\frac{Ju}{r\rho}\right) & \alpha_1 \frac{\partial}{\partial\eta}\left(\frac{J}{r\rho}\right) & \alpha_2 \frac{\partial}{\partial\eta}\left(\frac{J}{r\rho}\right) & 0 \\ \hline -\alpha_3 \frac{\partial}{\partial\eta}\left(\frac{Jv}{r\rho}\right) - \alpha_2 \frac{\partial}{\partial\eta}\left(\frac{Ju}{r\rho}\right) & \alpha_2 \frac{\partial}{\partial\eta}\left(\frac{J}{r\rho}\right) & \alpha_3 \frac{\partial}{\partial\eta}\left(\frac{J}{\partial\rho}\right) & 0 \\ \hline \alpha_4 \frac{\partial}{\partial\eta}\left[\frac{J}{r}\left(\frac{u^2+v^2}{\rho}\right) - \frac{e}{\rho^2}\right] & (\alpha_1-\alpha_4)\frac{\partial}{\partial\eta}\left(\frac{Ju}{r\rho}\right) & (\alpha_3-\alpha_4)\frac{\partial}{\partial\eta}\left(\frac{Jv}{r\rho}\right) & \alpha_4 \frac{\partial}{\partial\eta}\left(\frac{J}{r\rho}\right) \\ -\alpha_1 \frac{\partial}{\partial\eta}\left(\frac{Ju^2}{r\rho}\right) - \alpha_3 \frac{\partial}{\partial\eta}\left(\frac{Jv^2}{r\rho}\right) & +\alpha_2 \frac{\partial}{\partial\eta}\left(\frac{Jv}{r\rho}\right) & +\alpha_2 \frac{\partial}{\partial\eta}\left(\frac{Ju}{r\rho}\right) & \\ -\alpha_2 \frac{\partial}{\partial\eta}\left(\frac{Juv}{r\rho}\right) & & & \end{array}\right]$$

$$R_{i,j} = \left(\frac{J}{r\rho}\right)_{i,j} \left[\begin{array}{c|c|c|c} 0 & 0 & 0 & 0 \\ \hline (a_1 u + a_2 v)_{i,j} & -a_{1_{i,j}} & -a_{2_{i,j}} & 0 \\ \hline (a_3 v + a_2 u)_{i,j} & -a_{2_{i,j}} & -a_{3_{i,j}} & 0 \\ \hline -a_{4_{i,j}}\left(u^2+v^2-\frac{e}{\rho}\right)_{i,j} & (a_4 u - a_1 u)_{i,j} & (a_4 v - a_3 v)_{i,j} & -a_{4_{i,j}} \\ +(a_1 u^2 + a_3 v^2)_{i,j} & -(a_2 v)_{i,j} & -(a_2 u)_{i,j} & \\ +2(a_2 uv)_{i,j} & & & \end{array}\right]$$

$$Y_{i,j+1} = \left(\frac{J}{r\rho}\right)_{i,j+1} \begin{bmatrix} 0 & 0 & 0 & 0 \\ -(a_1 u + a_2 v)_{i,j} & -a_{1_{i,j+1}} & -a_{2_{i,j+1}} & 0 \\ -(a_3 v + a_2 u)_{i,j+1} & -a_{2_{i,j+1}} & -a_{3_{i,j+1}} & 0 \\ -a_{4_{i,j+1}} (u^2+v^2-\frac{e}{\rho})_{i,j+1} & (a_1 u - a_4 u)_{i,j+1} & (a_3 v - a_4 v)_{i,j+1} & -a_{4_{i,j+1}} \\ -(a_1 u^2 + a_3 v^2)_{i,j+1} & +(a_2 v)_{i,j+1} & +(a_2 u)_{i,j+1} & \\ -2(a_2 uv)_{i,j+1} & & & \end{bmatrix}$$

$$W_{i,j-1} = \left(\frac{J_{i,j-1}}{r\rho_{i,j+1}}\right) \begin{bmatrix} 0 & 0 & 0 & 0 \\ -(a_1 u + a_2 v)_{i,j} & -a_{1_{i,j-1}} & -a_{2_{i,j-1}} & 0 \\ -(a_3 v + a_2 u)_{i,j-1} & -a_{2_{i,j-1}} & -a_{3_{i,j-1}} & 0 \\ -a_{4_{i,j-1}} (u^2+v^2-\frac{e}{\rho})_{i,j-1} & (a_1 u - a_4 u)_{i,j-1} & (a_3 v - a_4 v)_{i,j-1} & -a_{4_{i,j-1}} \\ -(a_1 u^2 + a_3 v^2)_{i,j-1} & +(a_2 v)_{i,j-1} & +(a_2 u)_{i,j-1} & \\ -2(a_2 uv)_{i,j-1} & & & \end{bmatrix}$$

Matrices D, $\overline{M}_1$, $E_{i,j+1}$ and $E_{i,j-1}$ are given by

$$D = \frac{1}{r}\begin{bmatrix} 0 & 0 & 0 & 0 \\ 0 & 0 & 0 & 0 \\ \frac{\gamma-1}{2}(u^2+v^2) + \frac{4}{3}\frac{\mu v}{\rho r Re} & -(\gamma-1)u & -(\gamma-1)v - \frac{4}{3}\frac{\mu}{\rho r Re} & \gamma-1 \\ 0 & 0 & 0 & 0 \end{bmatrix}$$

$$\overline{M}_1 = \frac{1}{r}\begin{bmatrix} 0 & 0 & 0 & 0 \\ \frac{2}{3}\mu\eta_x\frac{v}{\rho} & 0 & -\frac{2}{3}\mu\frac{\eta_x}{\rho} & 0 \\ \frac{2}{3}\mu\eta_r\frac{v}{\rho} & 0 & -\frac{2}{3}\mu\frac{\eta_x}{\rho} & 0 \\ \frac{4}{3}\mu\frac{v}{\rho}(\eta_x u+\eta_r v) & -\frac{2}{3}\mu\eta_x\frac{v}{\rho} & -\frac{2}{3}\frac{\mu}{\rho}(u\eta_x+2v\eta_r) & 0 \end{bmatrix}$$

$$E_{i,j+1} = -\frac{1}{3}\frac{\mu}{ReJ}_{i,j}\begin{bmatrix} 0 & 0 & 0 & 0 \\ 0 & 0 & 0 & 0 \\ (\eta_x)_{i,j}\left(\frac{Ju}{r\rho}\right)_{i,j+1} + (\eta_r)_{ij}\left(\frac{Ju}{r\rho}\right)_{i,j+1} & (-\eta_x)_{ij}\left(\frac{Ju}{r\rho}\right)_{i,j+1} & (-\eta_r)_{ij}\left(\frac{J}{r\rho}\right)_{i,j+1} & \\ 0 & 0 & 0 & 0 \end{bmatrix}$$

$E_{i,j-1}$ is obtained by changing $i,\ j+1$ of $E_{i,j+1}$ to $i,j-1$.

APPENDIX C

Solution of Block Tridiagonal Systems

The use of the Beam and Warming implicit factored algorithm (23) in the solution of the thin layer Navier-Stokes equations leads to the inversion of tridiagonal systems. This appendix describes how the solution of such systems was obtained in this research.

Consider the following system:

$$\begin{bmatrix} Q_1 & N_1 & & & & & & \\ L_2 & Q_2 & N_2 & & & & & \\ & L_3 & Q_3 & N_3 & & & & \\ & & \cdot & \cdot & \cdot & & & \\ & & & \cdot & \cdot & \cdot & & \\ & & & & \cdot & \cdot & \cdot & \\ & & & & & L_{n-1} & Q_{n-1} & N_{n-1} \\ & & & & & & L_n & Q_n \end{bmatrix} \begin{bmatrix} x_1 \\ x_2 \\ x_3 \\ \cdot \\ \cdot \\ \cdot \\ x_{n-1} \\ x_n \end{bmatrix} = \begin{bmatrix} F_1 \\ F_2 \\ F_3 \\ \cdot \\ \cdot \\ \cdot \\ F_{n-1} \\ F_n \end{bmatrix} \tag{C1}$$

as may result from Equations (12) or (13) of the main text. Here, L_i, Q_i, and N_i are 4x4 matrices, and X_i and F_i are 4 element column vectors. Equation (C1) is rewritten as:

$$\underline{\underline{E}}\,\underline{X} = \underline{F}\ , \tag{C1a}$$

where "=" denotes a matrix and "-" a vector. A Lower-Upper decomposition of $\underline{\underline{E}}$ yields:

$$\begin{bmatrix} Q_1 & N_1 & & & & & \\ L_2 & Q_2 & N_2 & & & & \\ & L_3 & Q_3 & N_3 & & & \\ & & \cdot & \cdot & \cdot & & \\ & & & \cdot & \cdot & \cdot & \\ & & & & \cdot & \cdot & \cdot \\ & & & & & L_{n-1} & Q_{n-1} & N_{n-1} \\ & & & & & & L_n & Q_n \end{bmatrix} = \begin{bmatrix} I & & & & & & \\ \ell_2 & I & & & & & \\ & \ell_3 & I & & & & \\ & & \cdot & \cdot & & & \\ & & & \cdot & \cdot & & \\ & & & & \cdot & \cdot & \\ & & & & & \ell_{n-1} & I \\ & & & & & & \ell_n & I \end{bmatrix}$$

$$\times \begin{bmatrix} u_1 & N_1 & & & & & \\ & u_2 & N_2 & & & & \\ & & u_3 & N_3 & & & \\ & & & \cdot & \cdot & & \\ & & & & \cdot & \cdot & \\ & & & & & \cdot & \cdot \\ & & & & & & u_{n-1} & N_{n-1} \\ & & & & & & & u_n \end{bmatrix} \qquad \text{(C2)}$$

where u_i and l_i are 4x4 matrices, and I is the 4x4 unity matrix. Carrying out the multiplication on the right hand side of Equation (C2) and identifying terms, one obtains:

$$u_1 = Q_1 \qquad \text{(C3a)}$$

$$\ell_i = L_i \, u_{i-1}^{-1} \qquad \text{(C3b)}$$

$$u_i = Q_i - \ell_i \, N_{i-1} \qquad \text{(C3c)}$$

with $i = 2, 3, \ldots n$

Now replacing $\underline{\underline{E}}$ in Equation (C1a) by its Lower-Upper decomposition, carrying out the multiplication and identifying terms, one obtains:

$$g_1 = f_1 \tag{C4a}$$

and $$g_i = f_i - \ell_i g_{i-1} \quad , \quad i = 2, 3, \ldots n \tag{C4b}$$

$$X_n = u_n^{-1} g_n \tag{C5a}$$

$$X_i = u_i^{-1} (g_i - N_i X_{i+1}) \quad , \quad i = n-1 \ldots 2, 1 \tag{C5b}$$

Therefore, knowing u_i and l_i from Equations (C3) and g_i from Equations (C4), one may calculate the elements of $\underline{X}$ from Equations (C5). It should be noted that all required matrix inversions apply to 4x4 matrices and can be easily performed.

APPENDIX D

Boundary Conditions Extrapolation

The following sketch shows the boundary conditions specified for pipe flows.

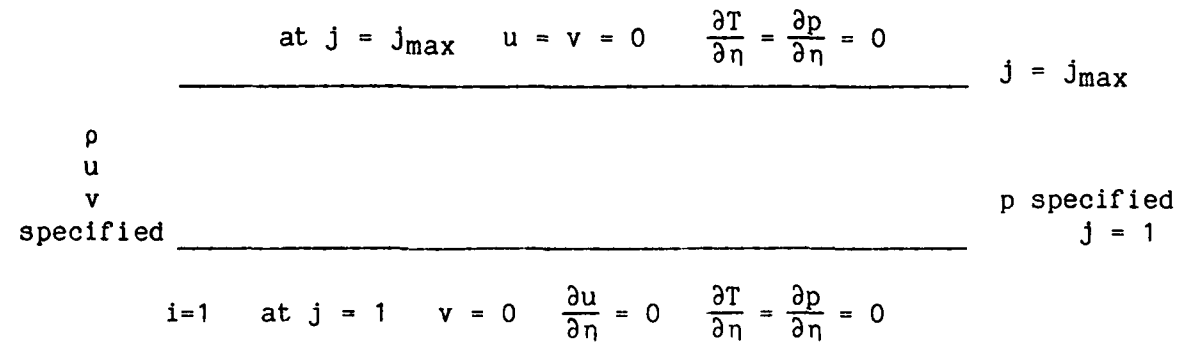

For the explicit part, the R.H.S. of Equation (10), at the inflow, the pressure p is obtained from linear extrapolation:

$$p_{i,j} = (1 + \frac{\Delta s_1}{\Delta s_2})\, p_{2,j} - \frac{\Delta s_1}{\Delta s_2}\, p_{3,j} \quad ,$$

where $\Delta s_1 = s_2 - s_1$, $\Delta s_2 = s_3 - s_2$ and s is the length along a ξ = constant line. The energy term, e, is obtained from the knowledge of ρ, u, v and p. At the outflow, u, v and ρ are obtained from an expression similar to the above extrapolation formula. At the wall, $j = j_{max}$, the following backward second order approximation is used to obtain T and p at wall from interior points.

$$\phi_\eta \Big|_{i,j_{max}} = \frac{3\phi_{i,j_{max}} - 4\phi_{i,j_{max}-1} + \phi_{i,j_{max}-2}}{2\Delta\eta} + O(\Delta\eta)^2,$$

where, $\frac{\partial p}{\partial \eta} = 0$ and $\frac{\partial T}{\partial \eta} = 0$ for an orthogonal grid.

At the centerline, or line of symmetry, $v = u_\eta = T_\eta = 0$ are specified. Again $\frac{\partial p}{\partial \eta} = 0$. The following second order approximation is used to obtain u, T and

p:

$$\phi_\eta\Big|_{i,1} = \frac{-3\phi_{i,1} + 4\phi_{i,2} - \phi_{i,3}}{2\Delta\eta} + O(\Delta\eta^2) \ .$$

For the implicit part of the algorithm, Equation (13) shows that at $j = j_{max}-1$, the knowledge of $N_{jm}\ \bar{q}^n_{i,jm}$ or a typical term such as $\bar{B}^n_{i,jm}\ \Delta\bar{q}^n_{i,jm}$ is required.

At the wall, $u = v = 0$ and the matrix multiplication of $(\tilde{B}^n\Delta\bar{q}^n)_{i,jm}$ yields the following:

$$(\gamma-1)\begin{bmatrix} 0 \\ (\eta_x\Delta\bar{e}^n)_{i,jm} \\ (\eta_r\Delta\bar{e}^n)_{i,jm} \\ 0 \end{bmatrix} \ .$$

For $p_\eta = 0$ one may approximate $\Delta\bar{e}_{i,jm}$ as follows.

$$\Delta\bar{e}_{i,jm} = \frac{4}{3}\left(\frac{r}{J}\right)_{i,jm}\left(\frac{J}{r}\Delta\bar{e}^n\right)_{i,j_m-1} - \frac{1}{3}\left(\frac{r}{J}\right)_{i,jm}\left(\frac{J}{r}\Delta\bar{e}^n\right)_{i,jm-2}$$

$$= a\ \Delta e^n_{i,jm-1} + b\ \Delta\bar{e}^n_{i,jm-2}$$

then

$(\tilde{B}^n\Delta\bar{q}^n)_{i,jm}$ may be rewritten as

$$\begin{bmatrix} 0 & 0 & 0 & 0 \\ 0 & 0 & 0 & (\eta_x)_{i,jm-1}(\gamma-1)a \\ 0 & 0 & 0 & (\eta_r)_{i,jm-1}(\gamma-1)a \\ 0 & 0 & 0 & 0 \end{bmatrix} \overline{\Delta q^n}_{i,jm-1} + \begin{bmatrix} 0 & 0 & 0 & 0 \\ 0 & 0 & 0 & (\eta_x)_{i,jm}(\gamma-1)b \\ 0 & 0 & 0 & (\eta_r)_{i,jm}(\gamma-1)b \\ 0 & 0 & 0 & 0 \end{bmatrix} \overline{\Delta q^n}_{i,jm-2}$$

In such a manner, $N_{jm}\ \overline{\Delta q}^n_{i,jm}$ is obtained as a linear combination of $\overline{\Delta q}^n_{i,jm-1}$ and $\overline{\Delta q}^n_{i,jm-2}$, which are the values at the interior points.

APPENDIX E

Computer Program

The computer program developed for the solution of the two dimensional (axisymmetric and planar) thin layer Navier-Stokes equations is presented in this appendix. The structure of the code is discussed, and a description of the code input variables is given. Output from the code is also described, and suggestions concerning how to run the code are given.

Code Description

The main routine of the code is very short, and merely allows to select between Equations (3), (4) or (5) of the text. It contains a parameter called IAXISY. For IAXISY = 0, Equation (4) is used. For IAXISY = 1, Equation (3) is used, and for IAXISY = 2, Equation (5) is used. For these three values of IAXISY, calls are made to Subroutines AXISY0, AXISY1 and AXISY2, respectively. These three subroutines are similar to each other in their internal structure: they all have an initialization part, or solution part, a boundary condition part and a wall correction part.

In the initialization part all constants and variables needed for the calculations are assigned values. A detailed description of input data is given below. During the initialization, a call is made to Subroutine TRANSF for the calculation of the finite difference grid. Also, during the initialization, initial values are given to the flow variables ρ, u, v, e, P (in the code, RHO2 (I,J), U2(I,J), V2(I,J), E2(I,J), P2(I,J)) in the entire flow field considered.

In the solution part, the right hand side of Equation (1) of the text (the $K_{i,j}$'s) is formed, with the explicit artificial viscosity terms included. The right hand side is stored in arrays HR(I,J), HM(I,J), HN(I,J) and HE(I,J). Then the ξ-sweep is carried out: matrices L_i, Q_i, and N_i (represented by

C(I, K1, K2), A(I, K1, K2) and B(I, K1, K2), where K1 and K2 have values from 1 to 4) are constructed, with the implicit artificial viscosity terms included, and the system of equations represented by Equation (12) of the text is solved. During the solution of Equation (12), a call is made to Subroutine TRIDIA which performs block tridiagonal inversions. Subroutine TRIDIA itself makes calls to Subroutine INVERT, which performs the inversion of 4 x 4 matrices. The solution of Equation (12) yields the $\Delta\bar{q}_{i,j}$'s, which are stored in HR(I,J), HM(I,J), HN(I,J) and HE(I,J) for use in the ξ-sweep. During the η-sweep, matrices L_j, Q_j and N_j are constructed with implicit artificial viscosity terms included, and a call to Subroutine TRIDIA leads to the solution of Equation (13) of the text for the $\Delta\bar{q}_{i,j}$'s.

In case the flow is turbulent, a call is made, at the beginning of the solution part, to Subroutine TURB or SUBROUTINE CEBECI, for the Baldwin-Lomax or the Cebeci turbulence model.

In the boundary condition part, the values of the flow variables are obtained at the boundaries according to the guidelines given in the text. Only the explicit treatment is done in this part, since the implicit treatment is involved in the formation of matrices L_i, Q_i, N_i and L_j, Q_j, N_j. In cases where scalar tridiagonal inversions are to be done (as in airfoil problems as explained in the text), Subroutine STRID is called.

The wall correction part is only used when an inverse design is desired, and only if the wall pressure residuals become smaller than Γ_p. When the secant method is used, a call is made to Subroutine SMOOTH, for the least squares smoothing of the computed geometries.

Subroutine TRANSF is the grid generation subroutine. In this subroutine, the coordinates of the boundary points are input and the coordinates of the interior modal points (X(I,J), R(I,J)) are obtained in two

ways: by interpolation from boundary points or by solution of elliptic partial differential equations (Appendix A). In addition, the grid may be read from a separate file (i.e. when the grid has been calculated from a different code and stored in a file). It is also possible to obtain a coarse, but smooth grid by solving the equations of Appendix A and refine it, say near a solid wall, by a spline interpolation procedure.

Input variables

The following is a description of the input variables, their meanings, and how they should appear on data cards. A complete description is first given for the planar case. Then changes related to the axisymmetric case are shown.

For the planar case, data are input as follows (M, L and all variables beginning with I or J are right justified integers):

Card 1

Column	Variable	Description
1-10	IAXISY	This flag is zero for planar flow. It is one for axisymmetric flow if Eq. (3) is used, and 2 if Eq. (5) is used. Eq. (3) should be used only for straight channels. Eq. (4) can be used for more complex shapes, but has not been tested for Re>100000.

Card 2

Column	Variable	Description
1-10	STEP	Time step for the numerical algorithm. Input in the form X.XXXE+XX, right justified.
11-20	Z	Numerical scheme selector. For the three-point-backward scheme, Z = 0.5.
21-30	THETA	Numerical scheme selector. For the three-point-backward scheme, THETA = 1.0.
31-40	M	Maximum number of grid points in the i-direction (ξ-direction). M should be less than 80.

41-50	L	Maximum number of grid points in the j-direction (η-direction). L should be less than 45.

Card 3

Column	Variable	Description
1-10	ITMAX	Maximum number of iterations (time steps) allowed.
11-20	IFREQ	Frequency with which intermediary data are output. If no intermediary output is desired, make IFREQ greater than ITMAX. If output of the dependent variables in the entire flow field is desired every 10 iterations, IFREQ = 10.
21-30	CRIT1	Value below which the density residual must fall for convergence.
31-40	CRIT2	Value below which the residual of ρu must fall for convergence.
41-50	CRIT3	Value below which the residual of ρv must fall for convergence.
51-60	CRIT4	Value below which the residual of e must fall for convergence.
61-70	CRIT5	Value below which the wall pressure residual must fall before a wall correction is made in design calculations. If no inverse design is desired, make CRIT5 smaller than CRIT1, CRIT2, CRIT3, CRIT4. CRIT1 to CRIT5 are input in the form X.XXE-XX and right justified.

Card 4

Column	Variable	Description
1-10	PO	Inlet stagnation pressure (Psia)
11-20	TO	Inlet stagnation temperature (°R).
21-30	AMACH	Inlet Mach number. For IFLAT=0, (see below), AMACH and the stagnation quantities are used to calculate the inlet velocity UINF, which is kept constant and is used as a reference velocity. The same thing applies when IFLAT=1 and IPOUT=0. For IFLAT=1 and IPOUT=1, this Mach number is discarded and recalculated from PO and POUT.
31-40	RAD	Characteristic length (i.e. chord length for airfoil, inlet radius for nozzle, diffuser,

		etc...) in feet. RAD is input in the form X.XXXE±XX.
41-50	ALPHA	Artificial viscosity coefficient for the explicit part (ε_1).
51-60	IVIS	IVIS=1 for viscous flow. IVIS=0 indicates an inviscid flow. However, adjustments have not been made for inviscid calculations.
61-70	IFLOW	Use zero if only grid computations are needed, and one if both grid and flow computations are needed.

Card 5

Column	Variable	Description
1-10	IREAD	Use zero if initial flow data are internally prescribed (usually uniform conditions) and one if initial flow data are read from a file.
11-20	ITURB	Use zero for laminar calculations and one for turbulent calculations.
21-30	IFLAT	Use one for airfoil calculations, and zero for flow between parallel plates, symmetric nozzles or diffusers, etc.. (where the centerline is a boundary).
31-40	INP	For IFLAT=0, use INP=0 if inlet conditions are internally prescribed (usually uniform conditions) and INP=1 if inlet velocity distribution is manually input. Not used if IFLAT = 1.
41-50	IPRT	Use IPRT=1 if initial flow data throughout the flow field are to be output, and IPRT=0 otherwise.
51-60	ISYM	Use ISYM=1 for symmetric airfoils at zero incidence angle and ISYM=0 otherwise. Not used for IFLAT=0.
61-70	ICASC	Use one for cascades, and zero for isolated airfoils. Not used for IFLAT=0.

Card 6

Column	Variable	Description
1-10	IB	Number of points along each periodic boundary in cascades. For isolated airfoils, IB=1.

11-20	IC	IB + number of points along the inlet boundary +1. For isolated airfoils, IC = M.
21-30	IG	Number of points along the wake boundary (between and including exit and trailing edge).
31-40	IGP	IG + Number of points along the airfoil surface (counting the trailing edge only once). IB, IC, IG and IGP are disregarded for IFLAT = 0.

Card 7

Column	Variable	Description
1-10	ITEMP	Use zero if temperature is not maintained fixed at the inlet, and one if it is (in which case velocity is also kept fixed at the inlet and pressure is extrapolated). Not used for IFLAT=0.
11-20	IPOTO	Use zero if stagnation pressure and stagnation temperature are not kept fixed at the inlet, and one if they are (in which case flow angle is prescribed and Riemann invariant is extrapolated). To maintain ρ, u and v fixed at the inlet, use ITEMP=IPOTO=0. For IFLAT=0, use ITEMP=IPOTO=0.
21-30	THIN	Prescribed angle between the inlet flow direction and the x-axis (degrees). Not used for IFLAT=0.
31-40	THOUT	Rough estimate of the exit flow angle (degrees). Used in internal calculation of initial velocity field. Not used for IFLAT=0.
41-50	XTE	The x-coordinate of the trailing edge, non-dimensionalized with chord length. Not used for IFLAT=0.

Card 8

Column	Variable	Description
1-10	ITWALL	Use zero for an adiabatic wall and one if wall temperature is prescribed. Not used for IFLAT=0.
11-20	TWALL	Prescribed wall temperature for ITWALL=1 (°R).
21-30	POUT	Prescribed exit pressure (Psia). Not used if IFLAT=1 and IPOUT=0.

31-40	IPOUT	Use IPOUT=1 if the exit pressure is input as POUT. Use IPOUT=0 if the exit pressure must be internally specified as the free stream pressure.

Card 3

Column	Variable	Description
1-10	INVERS	Use one if inverse calculation is desired, and zero otherwise.
11-20	NEWAL	For IFLAT=0, use NEWAL=0 for secant method and NEWAL=1 for virtual wall velocity method (for IFLAT=1 only virtual wall velocity method is used).
21-30	IDES1	Value of i corresponding to the beginning of the controlled region in inverse design. For IFLAT=0 use IDES1=1.
31-40	IDES2	Value of i corresponding to the end of the controlled region in inverse design. For IFLAT=0, use IDES2=M. For airfoil calculations, the controlled region must be on the upper surface, unless modifications to the code are made. For IFLAT=0 (and for the axisymmetric case), only the upper boundary (J=L) can be modified.
41-50	FACT	Multiplication factor used in smoothing for virtual wall velocity method (0.2 has been used).
51-60	RLOW	Minimum allowable value of wall distance from centerline in wall correction calculations with secant method. Used in smoothing, to discard erratic values.
61-70	RHIGH	Maximum allowable value of wall distance from centerline (see RLOW).

Card 10

Column	Variable	Description
1-10	IM	Same as M for grid calculations where ICLUS1=0 or when ISOREN=1 (see below).
11-20	IM	Same as L for grid calculations where ICALC=0 or ICLUST=0 or when ISOREN=1 (see below).
21-30	ITMAX	Maximum number of iterations for grid calculations.

31-40	ICALC	If ICALC=0, the grid is obtained by interpolation from specified boundary values. If ICALC=1, a PDE solution (APPENDIX A) gives the grid.
41-50	W	Relaxation coefficient in SOR solution of grid PDE's ($0 \leq W \leq 2.0$).

Card 11

Column	Variable	Description
1-10	ISOREN	If ISOREN=1, the grid is read from a file (e.g. a file obtained from Sorenson's program). If ISOREN=0, the grid is internally calculated.

Card 12 (skip if ISOREN=1)

Column	Variable	Description
1-10	ICLUST	For simple channels (diffusers, nozzles, etc...) the grid can be obtained as follows: calculate a coarse but smooth grid (ICALC=1) and then refine the grid by adding grid lines, say near the wall. If ICLUST=0, no grid refinement is needed. If ICLUST=1, the coarse grid is calculated using the input values of X(1,J) and R(1,J) (inlet coordinates). Then for the finer grid, a new distribution of the X(1,J)'s and R(1,J)'s must be given (the XG(J) and RG(J) values). With the new inlet distribution, the maximum number of points in the J-direction changes from JM to JMC. The new distribution of inlet points does not have to cover the entire inlet. For example, one may need to keep points from J=1 to J=JMLL as they are, and input a new distribution for J=JMLL+1 to J=JMC (see Figure E-1). The XG's and RG's are used to read in these JMC-JMLL values, and the grid in the rest of the domain is obtained by spline interpolation from the old grid.
11-20	JMC	Maximum number of points in J-direction for refined grid when ICLUST=1 is used. For ICLUST=1, JMC is equal to L.
21-30	JMLL	Number of inlet grid points (starting with J=1) which are left unchanged when a refined inlet distribution of points (ICLUST=1) is prescribed. If the refined distribution covers the whole inlet, make JMLL=1.

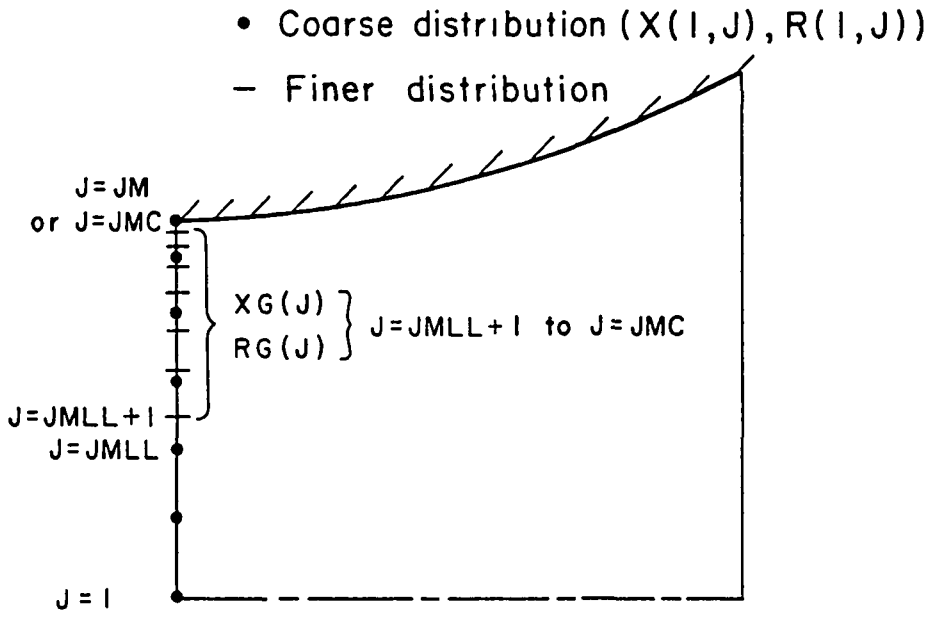

Figure E-1: Grid refinement option (ICLUST=1)

Card 13 (Skip if ISOREN=1)

Column	Variable	Description
1-10	ICLUS1	Similar to ICLUST, but applies to I-direction. Associated with IMC, IMLL, XGI(I), RGI(I). The ICLUS1 feature is not used for inverse design computations where grid computations are performed many times during the same run, after each wall correction.
11-20	IMC	Similar to JMC, but applies to I-direction. For ICLUS1=1, IMC is equal to M.
21-30	IMLL	Similar to JMLL, but applies to I-direction.

Card 14 (Skip if ISOREN=1)

Column	Variable	Description
1-10	P1	Initial value of f_1 (Eq. A4). A value of zero is usually used.
11-20	PX1	Coefficient a in Eq. (A4).
21-30	P2T	Initial value of f_2 (Eq. A4). A value of zero is usually used.
31-40	PX2	Coefficient c in Eq. (A4).

Card 15 (Skip if ISOREN=1)

Column	Variable	Description
1-10	Q1	Initial value of g_1 in Eq. (A4). A value of zero is usually used.
11-20	QX1	Coefficient b in Eq. (A4).
21-30	Q2	Initial value of g_2 in Eq. (A4). A value of zero is usually used.
31-40	QX2	Coefficient d in Eq. (A4).

Card 16 (Skip if ISOREN=1)

Column	Variable	Description
1-10	WP	Relaxation parameter in solution of grid equations ($0<WP\leq 2.0$).
11-20	WQ	Similar to WP
21-30	PLIM	Limitation factor to help stability of grid solution (PLIM=1.0 has been used).
31-40	QLIM	Similar to PLIM.

Card 16 (Skip if ISOREN=1)

Column	Variable	Description
1-10	WR	Similar to WP
11-20	WS	Similar to WP.
21-30	RLIM	Similar to PLIM
31-40	SLIM	Similar to PLIM.

Next input

. Values of X(I,1), the x values of grid points along the boundary J=1. IM values should be input, 5 per card, in 13 columns fields. Data are input in the form X.XXXXXXE±XX. All values are non-dimensionalized by characteristic length and are right justified. Skip if ISOREN=1.

. Values of R(I,1), the r values of grid points along the boundary J=1. IM values must be input. Skip if ISOREN=1.

. Value of X(I,JM), the x values of grid points along the boundary J=JM. IM values must be input. Skip if ISOREN=1.

. Values of R(I,JM), the r values of grid points along the boundary J=JM. IM values must be input. Skip if ISOREN=1.

. Values of X(1,J), the x values of grid points along the I=1 boundary. JM-2 values are needed (J=2 to J=JM-1). Skip if ISOREN=1.

. Values of R(1,J) the r values of grid points along the I=1 boundary. JM-2 values are needed (J=2 to J=JM-1).

. Values of X(IM,J), the x values of grid points along the I=IM boundary. JM-2 values are needed (J=2 to J=JM-1). Skip if ISOREN=1.

. Values of R(IM,J), the r values of grid points along the I=IM boundary. JM-2 values are needed (J=2 to J=JM-1). These values are used for the initialization but are not kept during the calculations. Skip if ISOREN=1.

. Values of XG(J), the x values of nodal points along the inlet boundary for refined grid. JMC-JMLL values are needed. Skip if ICLUST=0 or if ISOREN=1, or ICALC=0.

. Values of RG(J), the r values of nodal points along the inlet boundary for refined grid. JMC-JMLL values are needed. Skip if ICLUST=0 or if ISOREN=1, or ICALC=0.

. Values of XGI(I), the x values of nodal points along the J=1 boundary for refined grid. IMC-IMLL values are needed. Skip if ICLUS1=0 or ISOREN=1 or ICALC=0.

- Values of RGI(I), the r values of nodal points along the J=1 boundary for refined grid. IMC-IMLL values are needed. Skip if ICLUS1 = 0 or ISOREN=1 or ICALC=0.
- Values of PDES(I), the target pressure distribution, in Psia, for I=IDES1 to I=IDES2 (from I=1 to I=M for axisymmetric case). Skip if no design calculations are desired.
- Values of U2(1,J), the inlet velocity distribution, for J=1 to J=L, in ft/sec. Skip if INP=0.
- Values of the r coordinate at the wall (R(I,JM)) for second guessed geometry if secant method is used. Data are input for I=1 to I=M. Skip if secant method is not used.

In the above, all boundary data are input 5 per card, in the form x.xxxxxE+xx, and are right justified. Geometry data are non-dimensional.

For the axisymmetric case, data are input in the same way, except for the following cards:

Card 3

Column	Variable	Description
1-10	PINF	Exit static pressure, used as initial pressure everywhere (Psia)
11-20	TINF	Initial temperature, used as reference temperature (in °R).
21-30	UINF	Inlet velocity, used as reference velocity (in ft/sec).
31-40	RAD	See planar case.
41-50	ALPHA	See planar case.
51-60	IVIS	See planar case
61-70	IFLO	Same as IFLOW in planar case.

Card 4

Column	Variable	Description
1-10	ITURB	See planar case.
11-20	INP	See planar case.
21-30	IREAD	See planar case
31-40	IPRT	See planar case.

Card 5

Column	Variable	Description
1-10	ITEMP	Use ITEMP=0 if density is kept fixed at the inlet, and ITEMP=1 if temperature is kept constant. In both cases the inlet velocity is kept fixed and pressure is obtained by extrapolation.
11-20	TO	This stagnation temperature and UINF are used to obtain the static temperature which is maintained fixed at the inlet.
21-30	ICENT	Use ICENT=1 if the centerline is a boundary of the flow field (J=1) and ICENT=0 if there is a solid wall at J=1 (annular type). For ICENT=1, only laminar calculations can be performed, unless subroutine CEBECI is modified to account for two walls.

Card 6

Column	Variable	Description
1-10	INVERS	See planar case
11-20	NEWAL	See planar case
21-30	FACT	See planar case
31-40	RLOW	See planar case
41-50	RHIGH	See planar case

For the axisymmetric case, skip cards 7 to 9 of the planar case.

Output Description

The output of the code first shows all the input parameters in the order in which they are input. Reference quantities such as velocity,

density, temperature, viscosity, etc...., which are calculated by the code, are also printed.

Once the input parameters have been printed, the coordinates of the nodal points in the finite difference network are output: the X(I,J)'s are printed first, as M sets of data, each set corresponding to values of J from J=1 to J=JM. Then the R(I,J)'s are printed in the same manner. If ICALC=0, these values are the ones obtained by interpolation. If ICALC=1, these are the initial data for the grid computations. For ICALC=1, the residuals DELX and DELR for X and R are then printed for the first and the last iterations of the grid computations. Then the final distributions of the X(I,J)'s and the R(I,J)'s are printed.

If wall design calculations are to be done, the non-dimensional design pressure distribution (along the controlled portion of the solid wall to be modified) is printed next. If no design calculations are to be performed, the above is skipped and the initial velocity, density, pressure and energy fields are printed next if IPRT=1. The form of the output is the same as the form of the X(I,J) and R(I,J) output. The printed values are non-dimensional, and the title before each set of data indicates how the non-dimensional values can be used to obtain the dimensional values.

The residuals DEL1P, DEL2P, DEL3P, DEL4P and DEL5P are printed next. Residuals DEL1P to DEL4P are defined as the maximum differences between the values of ρ, ρu, ρv or e, respectively, between the current and the previous iteration in time (ITIME). DEL5P is defined the same way, but only applies to the wall pressure. Also printed are the locations (values of I and J such as IHR and JHR for ρ, IHM and JHM for ρu, IHN and JHN for ρv, IHE and JHE for e) where the maximum difference occurs. The residuals are printed for each iteration, and their overall trend should be decreasing.

If wall corrections are performed, the convergence history given by the above residuals will be interrupted whenever DEL5P becomes smaller than CRIT5. At this point, the wall pressure in the controlled region (corresponding to the current geometry) is printed. A new wall geometry is obtained, and the corresponding r-coordinates are printed. Also printed is DEL6P, the maximum difference between the current pressure and the target pressure. DEL6P is printed after every wall correction. However, it usually does not give an adequate indication on whether or not the current pressure is approaching the target pressure, since the wall correction scheme may not perform adequately at some points (such as the end points of the controlled region). A plot of the pressure distribution in the controlled region after each wall correction would give a better indication on the success of the wall correction scheme. For airfoil calculations, the calculations are stopped after each wall correction because a new grid must be externally obtained.

When DEL1P, DEL2P, DEL3P and DEL4P become smaller than CRIT1, CRIT2, CRIT3 and CRIT4, respectively (or after the number of iterations ITIME becomes larger than ITMAX), the calculations are stopped, and the final density, velocity, pressure and energy fields are output.

In addition to the output described above some data are automatically stored by the code on files. At the end of the grid calculations, the grid is stored in a data set with the reference number 13. At the end of the flow calculations, the entire flow field values of u, v, ρ, e, ρu, ρv, P are stored in a data set with the reference number 12. This way, the grid and flow data can be read from data sets 13 and 12 and used, for example, in a plotting routine written by the user.

Additional Considerations

The present code has been run in FORTRAN IV on an IBM 3081 computer. Double precision is used in the calculations. Adequate job control language statements must be provided in order to run the code.

As mentioned in the input data description section, a grid file is read by the code if ISOREN=1 and a flow field data file is read if IREAD=1. These files correspond to data set reference numbers 8 and 11, respectively. Adequate job control language statements must be incorporated to account for these input data sets. Also, in cases where the data sets are not available (which may be the case when IREAD=0 or ISOREN=0), if may still be necessary to create them (even if they contain no useful information) in order to make the execution possible.

As mentioned in the output description section, some data are stored in data sets 12 and 13. Adequate job control language statements must be incorporated to account for these output data sets. One interesting way of using data sets 11 and 12 would be, for example, to start the computations with IREAD=0. The final values of u, v, ρ, e, ρu, ρv for the calculation are automatically stored in a data set named DATA1 for example, corresponding to reference number 12. If more iterations are needed for convergence, one may restart the calculations using IREAD=1 and, through the appropriate job control language statements, associate data set DATA1 to reference number 11 and use a new data set name, i.e. DATA2, in association with reference number 12. Then for the new run, the initial flow field is read from 11 and the new results are stored in 12 (DATA2). This allows for a more efficient use of the code in very long calculations.

In order to read flow data stored by the code in a data set, a statement such as the following must be used:

```
      DO SN1 J=1,L
      DO SN1 I=1,M
SN1   READ(11,SN2), U2(I,J), V2(I,J), RHO2(I,J), E2(I,J), M2(I,J),
     1 N2(I,J), P2(I,J)
SN2   FORMAT(5X, 7E15.6)
```

In the above, SN1 and SN2 are statement numbers. The same format must be used in writing data into a file to be used by the code if IREAD=1. In order to read grid data stored by the code in a data set, a statement such as the following must be used:

```
      DO SN1 J=1,L
      DO SN1 I=1,M
SN1   READ(8,SN2), X(I,J), R(I,J)
SN2   FORMAT(2E14.6)
```

Sample Input and Output

The following is a simple example of a set of input data, and a computer plot of the velocity field (see Figure E-2). Notice that the plot was obtained by a small, separate code. Since plotting software varies with facilities, no plotting routine was incorporated in the code.

```
         2
0.500E+00     0.5         1.0              17          19
      450        1001  0.10E-04  0.10E-04  0.10E-04  0.10E-04  0.10E-05
    14.70      540.0       500.0     0.335E-02       2.0             1           1
           0           0           0           1
           1    542.0              1
           0           0    0.0         0.0         0.0
          17          11         100           1     1.55
           0
           1          19           1
           0           0           1
    0.0         0.3         0.0         0.7
    0.0         0.3         0.0         0.7
    0.3         0.3         1.0         1.0
    0.3         0.3         1.0         1.0
 0.00000E+00  0.12500E+00  0.25000E+00  0.37500E+00  0.50000E+00
 0.62500E+00  0.75000E+00  0.87500E+00  0.10000E+01  0.11250E+01
 0.12500E+01  0.13750E+01  0.15000E+01  0.16250E+01  0.17500E+01
 0.18750E+01  0.20000E+01
 0.00000E+00  0.00000E+00  0.00000E+00  0.00000E+00  0.00000E+00
 0.00000E+00  0.00000E+00  0.00000E+00  0.00000E+00  0.00000E+00
 0.00000E+00  0.00000E+00  0.00000E+00  0.00000E+00  0.00000E+00
 0.00000E+00  0.00000E+00
 0.00000E+00  0.12500E+00  0.25000E+00  0.37500E+00  0.50000E+00
 0.62500E+00  0.75000E+00  0.87500E+00  0.10000E+01  0.11250E+01
 0.12500E+01  0.13750E+01  0.15000E+01  0.16250E+01  0.17500E+01
 0.18750E+01  0.20000E+01
 0.10000E+01  0.10000E+01  0.10000E+01  0.10079E+01  0.10210E+01
 0.10342E+01  0.10473E+01  0.10604E+01  0.10736E+01  0.10867E+01
 0.10999E+01  0.11130E+01  0.11261E+01  0.11393E+01  0.11472E+01
 0.11472E+01  0.11472E+01
 0.00000E+00  0.00000E+00  0.00000E+00  0.00000E+00  0.00000E+00
 0.00000E+00  0.00000E+00  0.00000E+00  0.00000E+00  0.00000E+00
 0.10000E+00  0.20000E+00  0.30000E+00  0.40000E+00  0.50000E+00
 0.60000E+00  0.70000E+00  0.80000E+00  0.88000E+00  0.95000E+00
 0.20000E+01  0.20000E+01  0.20000E+01  0.20000E+01  0.20000E+01
 0.20000E+01  0.20000E+01  0.20000E+01  0.20000E+01  0.20000E+01
 0.10000E+00  0.20000E+00  0.30000E+00  0.40000E+00  0.50000E+00
 0.60000E+00  0.70000E+00  0.80000E+00  0.88000E+00  0.95000E+00
 0.00000E+00  0.00000E+00  0.00000E+00  0.00000E+00  0.00000E+00
 0.00000E+00  0.00000E+00  0.00000E+00  0.00000E+00  0.00000E+00
 0.00000E+00  0.00000E+00  0.00000E+00  0.00000E+00  0.00000E+00
 0.00000E+00  0.00000E+00  0.00000E+00
 0.15473E+00  0.30946E+00  0.45157E+00  0.56525E+00  0.65620E+00
 0.72896E+00  0.78717E+00  0.83374E+00  0.87099E+00  0.90079E+00
 0.92463E+00  0.94371E+00  0.95896E+00  0.97117E+00  0.98094E+00
 0.98875E+00  0.99500E+00  0.10000E+01
```

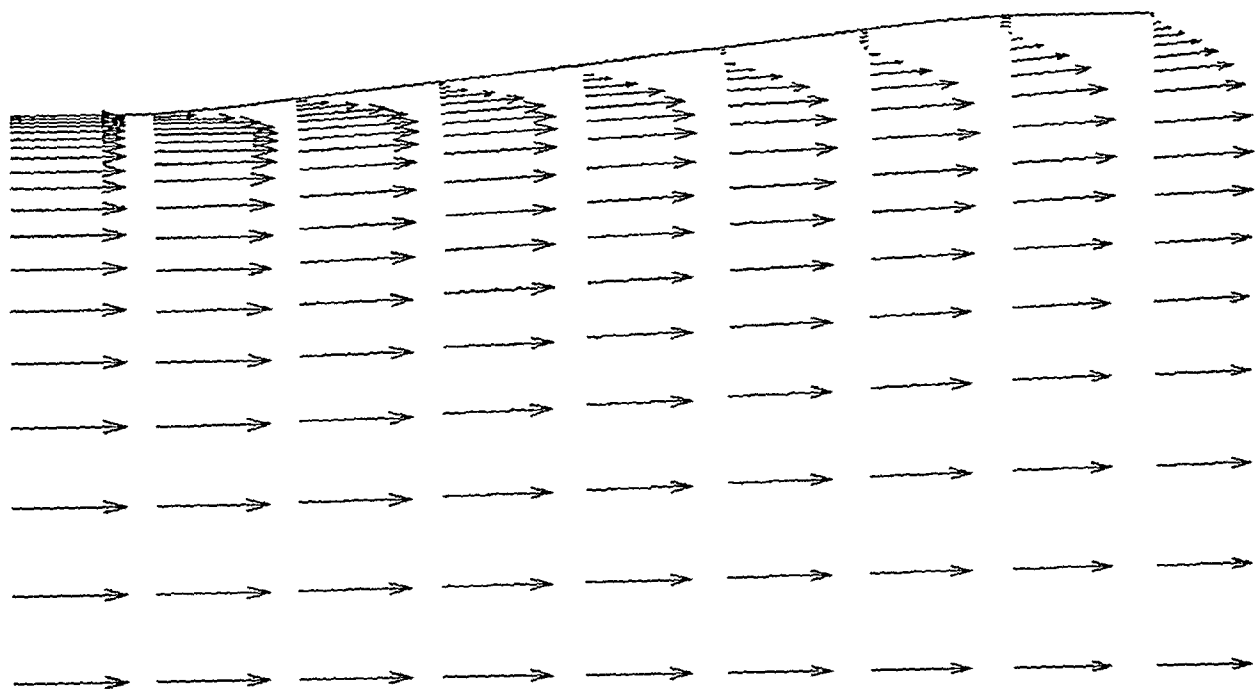

Figure E-2: Velocity field for axisymmetric laminar diffuser with an included angle of 12°. The inlet velocity is uniform at 500 ft/sec. The Reynolds number Re_d is approximately 20000.

1 Report No	2 Government Accession No	3 Recipient's Catalog No
NASA CR-175037		

4 Title and Subtitle	5 Report Date
Viscous Compressible Flow Direct and Inverse Computation with Illustrations	January 1986
	6 Performing Organization Code

7 Author(s)	8 Performing Organization Report No
Tah-Teh Yang and Francois Ntone	None
	10 Work Unit No

9 Performing Organization Name and Address	11 Contract or Grant No
Clemson University Mechanical Engineering Department Clemson, South Carolina	NAG 3-538
	13 Type of Report and Period Covered
12 Sponsoring Agency Name and Address	Contractor Report
National Aeronautics and Space Administration Washington, D.C. 20546	14 Sponsoring Agency Code
	505-62-21

15 Supplementary Notes

Final report. Project Manager, R.J. Steinke, Internal Fluid Mechanics Division, NASA Lewis Research Center, Cleveland, Ohio 44135.

16 Abstract

An algorithm for laminar and turbulent viscous compressible two-dimensional flows is presented. For the application of precise boundary conditions over an arbitrary body surface, a body-fitted coordinate system is used in the physical plane. A thin-layer approximation of the Navier-Stokes equations is introduced to keep the viscous terms relatively simple. The flow field computation is performed in the transformed plane. A factorized, implicit scheme is used to facilitate the computation. Sample calculations, for Couette flow, developing pipe flow, an isolated airflow, two-dimensional compressor cascade flow, and segmental compressor blade design are presented. To a certain extent, the effective use of the direct solver depends on the user's skill in setting up the gridwork, the time step size and the choice of the artificial viscosity. The design feature of the algorithm, an iterative scheme to correct geometry for a specified surface pressure distribution, works well for subsonic flows. A more elaborate correction scheme is required in treating transonic flows where local shock waves may be involved.

17 Key Words (Suggested by Author(s))	18 Distribution Statement
Viscous compressible flows; Computational fluid dynamics; Inverse solutions; Compressor cascade	Unclassified - unlimited STAR Category 07

19 Security Classif (of this report)	20 Security Classif (of this page)	21 No of pages	22 Price*
Unclassified	Unclassified	101	A06

*For sale by the National Technical Information Service, Springfield, Virginia 22161